

1 **Morphological and optical properties of carbonaceous aerosol particles from ship emissions and biomass burning during a summer cruise**
2 **measurement in the South China Sea**

3 **Cuizhi Sun¹, Yongyun Zhang¹, Baoling Liang^{1,&}, Min Gao¹, Xi Sun^{1,#}, Fei Li^{1,4}, Xue Ni¹, Qibin Sun¹, Hengjia Ou¹, Dexian Chen¹, Shengzhen Zhou^{1,2,3*},**
4 **and Jun Zhao^{1,2,3*}**

5 ¹ School of Atmospheric Sciences, Guangdong Province Key Laboratory for Climate Change and Natural Disaster Studies, and Southern Marine Science and
6 Engineering Guangdong Laboratory (Zhuhai), Sun Yat-sen University, Zhuhai, Guangdong 519082, China

7 ² Guangdong Provincial Observation and Research Station for Climate Environment and Air Quality Change in the Pearl River Estuary, Zhuhai, Guangdong
8 519082, China

9 ³ Key Laboratory of Tropical Atmosphere-Ocean System, Ministry of Education, Zhuhai, Guangdong 519082, China

10 ⁴ Xiamen Key Laboratory of Straits Meteorology, Xiamen Meteorological Bureau, Xiamen, Fujian 361012, China

11 [&] Now at Guangzhou Environmental Monitoring Center, Guangzhou, Guangdong 510060, China

12 [#] Now at Centre for Isotope Research (CIO), Energy and Sustainability Research Institute Groningen (ESRIG), University of Groningen, Groningen 9747
13 AG, the Netherlands

14 *Correspondence to:* Jun Zhao (zhaojun23@mail.sysu.edu.cn) and Shengzhen Zhou (zhoushzh3@mail.sysu.edu.cn)

15 **Abstract.** Carbonaceous aerosols constitute a crucial component of atmospheric marine aerosols among which black carbon (BC) and brown carbon (BrC)
16 are important contributors to light absorption and hence the positive climatic radiative forcing in the marine atmosphere. We conducted a month-long (May
17 05–June 09, 2021) onboard sample collections and online measurements of carbonaceous aerosols to characterize their morphological and optical properties
18 during a ship cruise in the South China Sea (SCS), covering a marine region of 11.9–24.5 °N and 111.1–118.2 °E. Single particles were collected by a single
19 particle sampler and offline analyses were performed using a transmission electron microscope (TEM) coupled with energy dispersive X-ray spectroscopy
20 (EDS). Online measurements of BC in PM_{2.5} were made by a seven-wavelength aethalometer and organic carbon (OC)/elemental carbon (EC) mass
21 concentrations were measured by a semi-online OC/EC analyzer. Feret diameters of the single particles during navigation and stop showed size distributions
22 with the lognormal fitting peaks at 307 and 325 nm, respectively. The fresh (without coating) and aged BC particles (after removal of coating by the electron
23 beams in TEM) showed same median fractal dimensions (1.61), in contrast to their different median lacunarities (0.53 vs 0.59). The aged BC particles showed
24 narrower Feret diameters (229–2557 nm) during navigation than those (78–2926 nm) of freshly-emitted BC from the own ship during stop. Moreover, tar

25 balls, as one important component of single particles from ship emissions and as the tracer of biomass burning, were identified with geometrical diameters of
26 160–420 nm in the TEM images. The EDS analyses showed those tar balls are mainly mixed with sea salt, organics, BC, and sulfate. We also found a
27 significant fraction of aged BC in various mixing states (core-shell, embedded) with other components of the aerosol particles after long-range transport.

28 The campaign was further divided into several periods (before monsoon period, BMP; transition monsoon period, TMP; after monsoon period, AMP; and
29 ship pollution period, SPP) according to the wind direction during monsoon and the own ship pollution. The median absorption Angström exponent (AAE)
30 values derived from all wavelengths were 1.14, 1.02, 1.08, and 1.06 for BMP, TMP, AMP and SPP, respectively. Particularly, a median AAE value of 1.93
31 was obtained during two significant biomass burning events. These results showed that biomass burning (BB) and fossil fuel (FF) combustion contributed to
32 18–22% and 78–82% of all the BC light absorption without the two intense biomass burning events, during which BB and FF accounted for 42% and 58%,
33 respectively. The two BB events originated from the Philippines and Southeast Asia before and after the summer monsoon. Our results demonstrated that BC
34 can serve as the core of aged particles but the fractal dimensions of BC aggerates were subject to little variation; moreover, such BC particles become much
35 more aggerated after aging in the marine atmosphere, which further affects the light absorption of the BC particles in the SCS.

36

37 **1 Introduction**

38 Carbonaceous aerosols (e.g., organic carbon (OC), elemental carbon (EC)/black carbon (BC)) profoundly impact regional and global climate (Corbin et al.,
39 2019; Lu et al., 2020; Rabha and Saikia, 2020). As an important component of carbonaceous aerosols, BC can serve as a tracer of anthropogenic pollution
40 once emitted from the incomplete combustion of fossil fuels and biomass burning. Moreover, BC particles are generally soot-aggregated with graphene-like
41 layer microstructures which can be observed under electron microscopy (Adachi et al., 2019). BC and EC are two components of carbonaceous aerosols that
42 are measured differently. BC is typically quantified based on its light-absorbing properties, while EC is measured using thermal-optical methods (Duarte et
43 al., 2021). However, EC can also be referred to as graphitic carbon or soot, with some overlap in their definitions. Another important component of
44 carbonaceous aerosols, BrC, represents a series of light-absorbing organic compounds, contributing significantly to the light absorption of atmospheric
45 aerosols (Wang et al., 2020b). BrC and BC show different light absorption patterns as a wavelength function. BrC and BC can be distinguished by measuring
46 the absorption spectra of aerosol particles at different wavelengths (Andreae and Gelencsér, 2006; Bond et al., 2013; Laskin et al., 2015; Li et al., 2020; Yus-
47 Díez et al., 2021). Tar balls are commonly used as typical tracers of biomass and biofuel burning due to their composition of amorphous carbon. These particles
48 also belong to BrC because they are light absorbing organics (Adachi et al., 2019; Hand et al., 2005). Spherical tar balls emitted from biomass burning have
49 been observed in cases of both wild fire burning (Adachi et al., 2019) and laboratory generated tar ball particles (Tóth et al., 2014). In the atmosphere, biomass
50 burning produces a significant amount of tar balls, which are not deliquescent but can absorb water at high relative humidity ($RH = \sim 80\%$), thereby affecting
51 their ability to scatter and absorb light (Hand et al., 2005).

52 The optical properties of BC and BrC particles are affected by several factors including the emission source, coating component, particle size, morphology,
53 and mixing state of the particles (Wei et al., 2020). The BC configuration in the single particles would influence their radiative effects (Luo et al., 2021). For
54 example, core-shell BC particles show enhanced light absorption compared to bare BC particles, especially when BC particles are coated with absorptive
55 materials such as BrC (Budhavant et al., 2020; Cappa et al., 2012; Shamjad et al., 2012; You et al., 2016). “Lensing effect” refers to the absorption enhancement
56 if BC is coated with non-absorbing organic or inorganic materials (Luo et al., 2021; Yang et al., 2009). In contrast, if the BC coating materials are highly
57 absorptive, no absorption enhancement may occur at shorter visible and UV wavelengths, a phenomenon known as “shielding effect”. The shielding and
58 lensing effects depend on the coating thickness over BC (Lack and Cappa, 2010). When BC is well internally mixed with BrC, its total absorption enhancement
59 becomes smaller than the enhancements of not well mixed counterparts due to the absorptive coating that acts as a shield (Feng et al., 2021). Moreover, it is
60 impossible for BC and other materials to be homogeneously distributed.

61 The extent to which BC and BrC contribute to light absorption in atmospheric aerosols can be assessed using the absorption Ångström exponent (AAE)
62 (Wang et al., 2020a). AAE is a parameter used to quantify the spectral dependence of aerosol light absorption. It is calculated by fitting a power-law relationship
63 between the aerosol absorption and wavelengths over a given spectral range. The AAE is used to identify sources and types of aerosols and a higher AAE
64 value is associated with sources such as biomass burning or urban pollution, while a lower AAE value suggests absorption by larger particles, such as mineral
65 dust or sea salt (Blanco-Donado, 2022; Duarte et al., 2021). However, many factors such as mixing state, coating, particle size, refractive index, wavelength,
66 and emission source, would affect the AAE values for BC and BrC aerosols, leading to large variations among different studies (Moschos et al., 2021). For
67 example, a previous study showed that the AAE values derived from wavelengths of 405 and 781 nm are very sensitive to refractive index and particle
68 diameter (Chylek et al., 2019). The AAE values of 0.8–1.6 at 470 and 950 nm are attributed to traffic emissions and fuel combustion (Ezani et al., 2021).
69 Comparatively, those AAE values can be as large as 2.0 for ship emissions (Helin et al., 2021). Moreover, the recommended AAE value for fossil fuel (FF)
70 and biomass burning (BB) is 1 and 2 (or higher), respectively (Liu et al., 2023). Other AAE values were also found in previous studies for FF (0.9) and BB
71 (1.68) (Zotter et al., 2017) or FF (1.2) and BB (2.2) as the mostly used optical pair (Milinković et al., 2021). The AAE values of 1.4 and 1.7 for BC and BrC
72 were set to be the lower and upper limits in the modelling study of biomass burning particles mixed with BC and BrC (Chylek et al., 2019). However, the use
73 of constant AAE values for calculating the BC fractions from BB and FF led to large uncertainties without knowledge of the core size or coating thickness of
74 the BC particles (Virkkula, 2021). Currently, the effect of the light absorption is not well known for the carbonaceous particles in the marine atmosphere due
75 to scarce ship-based measurements.

76 The optical properties of BC and BrC particles can also be investigated through fractal dimension (D_f) analysis based on the fractal properties of BC
77 aggregates. D_f illustrates how particles aggregate and grow and it can be determined through boxing counting calculation, ensemble method, or soot parameter
78 method with TEM images (Pang et al., 2022). The D_f values are mainly related to emission sources and aging process of the particles. Previous studies showed
79 that the D_f values of fresh BC particles tend to be small but become larger after aging because the particles are more compact due to coatings (Luo et al., 2022;
80 Wang et al., 2017). D_f values of 1.8 and 2.6 were used respectively for fluffy and compact BC particles in a numerical study to investigate the impact of the
81 BC morphology on light absorption (Luo et al., 2021). Laboratory experiments simulating wildfires showed that the D_f values of freshly emitted BC were in
82 a range of 1.74–1.92 (Chakrabarty et al., 2006), compared to the range of 1.67–1.83 from a field study of the Las Conchas fire (China et al., 2013). A similar
83 range of the D_f values of 1.67–1.93 were found at a remote site in the southeastern Tibetan Plateau (Wang et al., 2017). The obtained D_f values for the traffic
84 emissions were as large as 3 (Wei et al., 2020). In addition to the emission sources and aging process, D_f is also dependent on the particle size. A previous
85 experimental study found that for polystyrene latexes (PSL) particles, the D_f values decreased with the increase of particle size up to 200 nm (Wu et al.,

86 2013b). Nevertheless, knowledge of the fractal dimension for carbonaceous particles in the marine atmosphere is currently very limited, hindering our ability
87 to understand the aging process and the optical properties of these particles.

88 In the past years, carbonaceous aerosols in the marine atmosphere have been extensively studied on regional and global scales, focusing on the transport of
89 anthropogenic emissions to the sea areas. The BC background concentrations in Antarctic and Arctic regions are below 20 ng m^{-3} (Fossum et al., 2022). The
90 BC outflows from Asia to the Pacific Ocean exhibit seasonal variations and originate from anthropogenic and biomass-burning sources in China, Siberia, and
91 Southeast Asia (Matsui et al., 2013). Ship-based BC and EC measurements reveal significant influence of continental transport on remote oceanic regions,
92 including the Bay of Bengal (Kedia et al., 2012), Indian Ocean (Kompalli et al., 2021), Southern Indian Ocean and the Southern Ocean (Ueda et al., 2018),
93 North Sea (Bencs et al., 2020), Antarctic (Chaubey et al., 2013; Schmale et al., 2019), North Pacific (Taketani et al., 2016; Xing et al., 2014), Arctic (Pankratova
94 et al., 2021; Sharma et al., 2019), Northeast Atlantic (Fossum et al., 2022), the Yellow Sea (Kwak et al., 2022), and Western Pacific (Ma et al., 2022). However,
95 to our knowledge, the BC mass concentrations have been found to vary significantly across different oceans and seasons, with levels from 3 to 2800 ng m^{-3}
96 and being influenced by anthropogenic activities and seasonal factors. The online BC measurements in the South China Sea (SCS) region are limited. An
97 early study reported BC concentrations on Yongxing Island during the rainy season (May 16–June 20, 2008) and the dry season (Dec. 12, 2008–Jan. 8, 2009),
98 with average concentrations of 0.54 and $0.67 \mu\text{g m}^{-3}$, respectively (Wu et al., 2013a). Recent studies conducted at coastal sites in the SCS found that BC
99 concentrations are strongly impacted by land anthropogenic emissions (Wang et al., 2022). The time-resolved BC concentration varies with the vertical heights
100 (Sun et al., 2020c) and the carbonaceous materials of OC and EC account for 31–62% in $\text{PM}_{2.5}$ (Yan et al., 2018). Nevertheless, quantification of the light
101 absorption potential of BC and BrC aerosols remains challenging due to the limited knowledge regarding the morphology, particle size, and mixing state of
102 carbonaceous particles in the SCS (Kompalli et al., 2021). Furthermore, the atmosphere in the SCS is typically influenced by the southwesterly monsoon from
103 May to August (Wang and Wu, 2020), which affects the air masses from Southeast Asia. In this study, we conducted ship-based measurements of BC, OC/EC,
104 and single particle sampling during summer (May 05–June 09, 2021) in the SCS. The morphology (i.e., the fractal dimension and the size of the single BC
105 particles) and light absorption properties of carbonaceous particles were characterized. The source origins, relationships between the D_f and BC size, as well
106 as the impact of summer monsoon on the light absorption of the BC particles are discussed.

107 2 Methods

108 2.1 Cruise route and instrumentation

109 The cruise measurements were carried out from May 5 to June 9, 2021, covering a marine area of 11.9–24.5 °N and 111.1–118.2 °E in the SCS. Single
110 particles were collected on the TEM grids (3.05 mm I.D., copper meshed and covered with lacey carbon film) located on the front deck during ship navigation
111 and stop using a single-stage particle sampler (DKL-2, Genstar Electronic Technology Co., Ltd., China) which is the same as other studies (Chen et al., 2023;
112 Dong et al., 2018; Liu et al., 2021; Pang et al., 2022). The sampling flow rate and time were set at 1 L min⁻¹ and 10 min, respectively, for each collection. The
113 nozzle diameter of this single-cascade impactor is 0.3 mm. The particles with aerodynamic diameters above 0.2 μm were collected with a collection efficiency
114 of 50%, assuming a particle density of 1.5 kg m⁻³ (Marple and Olson, 2011). More details can be found in the supplementary information (Section 1 of SI).
115 The mixing state and morphology of the single particles were analyzed utilizing a transmission electron microscope (TEM, FEI Tecnai G2 Spirit, Holland)
116 operated at an accelerating voltage of 120 kV, in conjunction with an energy dispersive spectrometer (EDS, Bruker Nano GmbH Berlin, Esprit 1.9, Germany)
117 for elemental analysis. The thickness of the EDS detector (type XFlash 5060) is 0.45 mm with a Si dead layer of 0.029 mm. Notably, in the EDS spectra,
118 when analyzing particle composition, Cu should be excluded, and a considerable level of C and Si should be observed in the background signals due to the
119 presence of Si in the detector, Cu and C in the TEM grid. The substrate holder of TEM was tilted 25° for thorough inspection during imaging and EDS analysis.

120 The sampling inlets were installed on the bow of the research vessel with a height of ~ 15 m above sea level. The own ship emissions (e.g., engine, cooking,
121 etc.) were exhausted from the chimney on the stern with a linear distance of ~ 22 m to the inlets. The BC mass concentrations were measured by an aethalometer
122 (Model AE33, Magee Scientific, USA) with a time resolution of one minute (Drinovec et al., 2015). Note that the BC mass concentrations derived from AE33
123 are referred to as equivalent BC mass concentrations due to the light absorption of both BC and BrC at 880 nm. The sampling air was regulated by a PM_{2.5}
124 cyclone (BGI Inc., Waltham, MA, USA) and subsequently dried by a Nafion dryer (Model MD-700 series, Perma Pure Inc., USA) with a relative humidity
125 below 40% through the filter tape (type 8060) at a sample flow rate of 5 L min⁻¹. Data corrections were made for the employed Aethalometer AE33, considering
126 the multiple scattering parameters ($C(\lambda)=1.39$) for the used filter type, the leakage factor ($\zeta=0.01$), and the compensation parameters ($K_{\min}=-0.005$, $K_{\max}=0.015$).
127 The measured attenuation at seven wavelengths (7 channels) is used to determine the wavelength-dependent absorption coefficient. The mass specific
128 absorption cross-sections (MAC, σ_{air}) applied in the BC calculations were 18.47, 14.54, 13.14, 11.58, 10.35, 7.77, and 7.19 m² g⁻¹ for wavelengths of 370,
129 470, 520, 590, 660, 880, and 950 nm, respectively (Ausmeel et al., 2020). The measured values at 880 nm (channel 6) are for black carbon concentration
130 calculation, and at 370 nm (channel 1) for UV particulate matter (UVP) concentration (Drinovec et al., 2015). The detection limit of AE33 aethalometer is

131 approximately $0.03 \mu\text{g m}^{-3}$ for 1-min integration period and below $0.005 \mu\text{g m}^{-3}$ for 1-hour integration period. The instrument was automatically calibrated by
132 zero air every day. Notably, significant spikes were observed during periods when the ship was stationary, when it was travelling at low speeds, and when the
133 wind was blowing from the stern of the vessel.

134 The OC/EC concentrations were measured by a semi-continuous OC/EC analyzer (Model-4, Sunset Laboratory Inc., USA) based on the optical attenuation
135 and thermo-optical transmittance methods (Geron, 2009) under the NIOSH 5040 thermal-optical protocol (Lappi and Ristimäki, 2017). Similarly, the sampling
136 air passed through a $\text{PM}_{2.5}$ cyclone (BGI Inc., Waltham, MA, USA) and was dried by a Nafion dryer (Model MD-700 series, Perma Pure Inc., USA) with a
137 relative humidity below 40% at a flow rate of 8 L min^{-1} . The air then passed through a denuder for the removal of volatile organic compounds (VOCs) and
138 the particles were collected on the quartz filter with 45-min accumulation and 15-min analysis. The instrument was calibrated with the standard sucrose
139 solution as recommended. The manufacturer-claimed detection limits are 0.4 and $0.2 \mu\text{g m}^{-3}$ for OC and EC, respectively (Brown et al., 2019). However,
140 several previous studies showed that these values may vary substantially in a range of 0.04 – 2 and 0.001 – $0.5 \mu\text{g m}^{-3}$ for OC and EC, respectively, due to the
141 artifact of the quartz filters (Bao et al., 2021; Bauer et al., 2009; Chen et al., 2017; Jung et al., 2011; Karanasiou et al., 2020; Park et al., 2018; Zhang et al.,
142 2021). Here, we estimated the instrument noise (including contamination) of 0.15 and $0.012 \mu\text{g m}^{-3}$ for OC and EC based on 26 effective blank measurements
143 with 3 times the standard deviation (3σ) during the campaign. The limit of detection (LOD) for OC and EC is 0.18 and $0.19 \mu\text{g m}^{-3}$, respectively, calculated
144 as three times the standard deviation of replicate measurements of a standard sucrose solution with a carbon content of $10.516 \mu\text{g m}^{-3}$. The Sunset OC/EC
145 analyzer also measures optical EC based on the transmission of 660 nm wavelength light through the quartz fiber filter employed for sampling, similar to the
146 AE33 for optical BC measurements. Optical EC is defined as the apparent EC on the filter based on the measured apparent absorbance and the fixed absorption
147 coefficient according to the user's manual of the Sunset OC/EC. Both our study and a previous study (Brown et al., 2019) showed that the optical EC
148 concentrations from Sunset were comparable with the BC concentrations from AE33. Note that the resultant optical EC concentrations from the instrument
149 output may be overestimated due to the limitation of the filter-based optical measurements.

150 The measurements of solar radiation (SR), temperature (T), pressure (P), relative humidity (RH), relative wind direction (RWD), and relative wind speed
151 (RWS) were provided by the automatic weather station (AWS430, Vaisala Inc., Finland) (Song et al., 2022) equipped on the front deck of the research vessel.
152 This station comprises a range of integrated sensors, including a wind speed and direction sensor (model WMT702), a temperature and humidity sensor (model
153 HMP155), and an atmospheric pressure sensor (model BARO-1). The cruise route for ship navigation is from the global positioning system (GPS) onboard
154 the ship (Seapath 330+, Kongsberg Inc., Norway).

155 2.2 Data analyses and processing

156 2.2.1 Analyses of single particles

157 A total of 34 samples (15 during navigation and 19 at stop) were analyzed and more than 20 bright-field TEM images were randomly captured for each sample
158 except for those at the center of the grids where particles were easily overlapped. A total of 15624 single particles were statistically analyzed to obtain
159 morphology information (i.e., the Feret diameter, area, perimeter) for each particle using the software ImageJ (1.53q, National Institute of Health, USA)
160 (Cheng et al., 2021). In the analysis of particle size, the Feret diameter is defined as the distance between the parallel tangential lines that constrain the particle
161 perpendicularly. In this study, we applied the Feret diameter as the longest distance between any two points along the boundary of the selected particles.
162 Moreover, we utilized “geometrical diameter” to describe the size of tar balls with circular shape, which signifies the distance between two points located on
163 the surface of a geometric shape, with this line passing through the shape's center. Using “Geometrical diameter” is suitable to quantify the size of the observed
164 tar balls which excluded any coatings or additional materials. Specifically, we employed TEM data acquisition software to measure the geometrical diameters
165 of observed tar balls. The D_f values of the BC particles were estimated using the boxing counting method using the plugin Fraclac. An example was given in
166 the SI (section 2, Fig. S1) to show how to calculate D_f using the software. A detailed description of the procedure using the boxing counting method and the
167 software ImageJ can be found in the SI. The D_f values are very sensitive to the fill extent and sizes of the particles. A previous study showed low fractal
168 dimensions when the particles contain void volumes (Peyronel et al., 2010).

169 The own ship emissions can be identified using various measures, for example, high CO, NO_x concentrations (Sun et al., 2020b), high BC concentrations
170 (Alroe et al., 2019; Shank et al., 2012), regular cooking emissions (Cai et al., 2020), and wind speeds/directions between the ship stop and start operation
171 (Ausmeel et al., 2020; Kwak et al., 2022). The contribution of ship emissions to BC sources on the marine atmosphere depends on engine types, operation
172 modes, fuel types, and loadings (Gagne et al., 2021; Jiang et al., 2018; Karjalainen et al., 2022; Lack and Corbett, 2012; Wu et al., 2021; Zhao et al., 2020).
173 Here, we classify two sampling modes (navigation vs stop) of single particle analyses according to ship operation, and relative wind direction/speed. In this
174 study, the relative wind direction/speed is relative to the ship heading. The navigation mode is constrained by the relative wind direction of 0–80° or 280–
175 360°, and the relative wind speed greater than 5 m s⁻¹, averaged for every 10 minutes (consistent with the collection time of TEM samples). The stop mode is
176 set with the relative wind direction of greater than 80° and less than 280°, or the relative wind speed lower than 5 m s⁻¹. The navigation mode samples are
177 mainly from marine air and air masses of long-range transport while the stop mode collected air masses which are mixed with the own ship emissions. The
178 wind direction (speed) and relative wind direction (speed) are calculated by Eq. (1) (Aijjou et al., 2020).

179
$$V_R = \sqrt{V_s^2 + V_w^2 + 2 * V_s * V_w * \cos \alpha} \quad (1)$$

180 where V_R is the relative wind direction (speed), V_s is the ship direction (speed), V_w is the true wind direction (speed), α is the angle between the ship
 181 heading and the true wind direction.

182 The temporal profiles of ship heading directions, and relative wind direction/speed are shown in the SI (section 3, Fig. S2). Details of the two sampling
 183 modes (navigation vs stop) on a vector average of 10 minutes are listed in Table S1 and Fig. S3. Here, we distinguished the own ship emissions (research
 184 vessel) from those of other ships or long-range transport based on the following criteria: low relative wind speed ($< 5 \text{ m s}^{-1}$), relative wind direction
 185 encompassing ship exhaust ($80\text{--}280^\circ$), and a substantial AE33-derived hourly averaged BC mass concentration ($>2 \mu\text{g m}^{-3}$). Other ship emissions far from the
 186 research vessel are treated as a part of the transported air masses in this study.

187 2.2.2 BC, OC, EC and optical EC data

188 In this study, BC data obtained from the AE33 instrument are referred to as BC, while data from the OC/EC analyzer is expressed as thermal OC, thermal EC,
 189 and optical EC. Here, we averaged the BC mass concentrations over one minute and excluded those below the detection limit of $0.03 \mu\text{g m}^{-3}$ to minimize the
 190 variations. We also removed the own ship emissions which are characterized by spikes in particle number concentrations according to the wind directions
 191 (Fossum et al., 2022). BC mass concentration was calculated using Eqs. (2, 3) which are cited from the AE33 aethalometer user's manual (Ver 1.54).

192
$$ATN = -100 * \ln (I/I_0) \quad (2)$$

193 where ATN is optical attenuation, I_0 is reference signal, I is spot signal.

194
$$BC = \frac{S * (\Delta ATN_1 / 100)}{F_1 (1 - \zeta) * \sigma_{air} * C * (1 - k * AN T_1) * \Delta t} \quad (3)$$

195 where BC is black carbon concentration, S is spot area, F_1 is measured flow, ζ is leakage factor, σ_{air} is the mass absorption cross-section (MAC), C is multiple
 196 scattering parameter, k is compensation parameter, and t is time.

197 AAE was calculated according to Eq. (4) using the light absorption at wavelengths of 470 and 950 nm, which are built-in algorithms in the AE33
 198 aethalometer as described elsewhere (Helin et al., 2021; Kang et al., 2022; Milinković et al., 2021; Zotter et al., 2017). This method serves as a two-composition
 199 source apportionment for BC emitted from fossil fuels and biomass burning (AAE model), which applied AAE=1 for fossil fuel and AAE=2 for biomass. The
 200 calculations for BC(BB) and BC(FF) are shown in Eqs. (5–7) which are referred to the AE33 aethalometer user's manual and publication (Sandradewi et al.,
 201 2008). The optical absorption coefficient is the sum of biomass burning and fossil fuel burning contributions. Basic equations are using Beer-Lambert's Law.

$$AAE = -\frac{\ln\frac{\sigma_{abs}(\lambda_1)}{\sigma_{abs}(\lambda_2)}}{\ln\frac{\lambda_1}{\lambda_2}} \quad (4)$$

where σ_{abs} is aerosol absorption coefficient, σ_{air} is mass absorption cross-section (MAC), $\sigma_{abs} = BC * \sigma_{air}$. $\lambda_1 = 470$ nm and $\lambda_2 = 950$ nm.

$$\frac{\sigma_{abs}(470\text{ nm})_{FF}}{\sigma_{abs}(950\text{ nm})_{FF}} = \left(\frac{470}{950}\right)^{-AAE_{FF}} \quad (5)$$

$$\frac{\sigma_{abs}(470\text{ nm})_{BB}}{\sigma_{abs}(950\text{ nm})_{BB}} = \left(\frac{470}{950}\right)^{-AAE_{BB}} \quad (6)$$

$$\sigma_{abs}(\lambda) = \sigma_{abs}(\lambda)_{FF} + \sigma_{abs}(\lambda)_{BB} \quad (7)$$

where $\sigma_{abs}(470\text{ nm})_{FF}$ and $\sigma_{abs}(950\text{ nm})_{FF}$ are the aerosol absorption coefficients at wavelengths of 470 and 950 nm for fossil fuel (FF), $\sigma_{abs}(470\text{ nm})_{BB}$ and $\sigma_{abs}(950\text{ nm})_{BB}$ are the aerosol absorption coefficients at wavelengths of 470 and 950 nm for biomass burning (BB), AAE_{FF} and AAE_{BB} are equals to 1 and 2, respectively.

Alternatively, AAE can be obtained from the negative slope of linear regression between the log-transformed σ_{abs} and all the wavelength spectra so that hourly AAE values (all λ) can be obtained following a similar method in Retama et al. (2022). Details are shown in the SI (Section 4, Figure S4). Here, we define Delta-C as the difference between the concentration derived from the aforementioned UVPM data (at 370 nm) and BC concentration (at 880 nm). This Delta-C parameter was employed as an indicator of smoke from biomass burning in previous wood biomass burning studies (Harrison, 2020; Zhang et al., 2017).

The OC and EC (thermal) concentrations lower than the instrument noise (0.15 and 0.012 $\mu\text{g m}^{-3}$ for OC and EC, respectively) were excluded. Additional data were removed for those with laser correction factors below 0.88 and calibration peak areas lower than the initial calibration levels (within 10%), and a total of 551 h data were used for further analysis. In comparison, the Sunset optical EC (at 660 nm) is generally consistent with the Magee AE33 aethalometer derived BC (at 880 nm) within 9% (Brown et al., 2019) which is shown in Section 3.3. The EC concentration data from Sunset were considered as ship pollution and were discarded when the BC concentrations from the AE33 aethalometer were higher than 2 $\mu\text{g m}^{-3}$, in addition to those with relative wind directions of 80–280° regardless of the BC concentrations as mentioned before.

2.2.3 HYSPLIT backward trajectory and MODIS fire data

The backward trajectories were calculated using NOAA HYSPLIT (Hybrid Single-Particle Lagrangian Integrated Trajectory) (Version 5) at heights of 100, 500 and 1000 m above sea level (AGL). Daily meteorological data with 1.0°×1.0° spatial resolution for trajectory calculation were downloaded from the global data assimilation system (GADS) (<ftp://arlftp.arlhq.noaa.gov/pub/archives/gdas1/>). Here, we calculated the 72-h back trajectories of air masses arriving

225 at the single particle sampling sites along the cruise route.
226 Moderate Resolution Imaging Spectrometer (MODIS) data are available from the Near real-time MODIS Collection 6 products
227 (<https://firms.modaps.eosdis.nasa.gov/download/>). Here, we selected a region of 102–127 °E and 0–30 °N fully covering the campaign area. The number of
228 fire hotspots was counted each day during the campaign with a confidence level of higher or equal to 80% as recommended (Giglio et al., 2020). A detailed
229 description of the fire detection algorithms is available online (<https://earthdata.nasa.gov/what-is-new-collection-6-modis-active-fire-data>).

230 **3 Results and discussion**

231 **3.1 Overview**

232 Figure 1 shows the time series of ship cruise route and the single particle sampling locations during ship navigation (marked as solid triangles) and stop
233 (marked as open squares) over the SCS during the campaign. The cruise sequences are AB→C→D→EB→D→A, with AB and EB being non-stop cruise,
234 otherwise the ship stopped occasionally along the arrow routes for other research tasks. Figure 2 shows the time series of the meteorological variables (i.e.,
235 solar radiation (SR), temperature, pressure, relative humidity (RH), wind direction (WD), and wind speed (WS) during the whole campaign (May 05–June
236 09, 2021). The measurements were conducted mostly on sunny days prior to June 02 as shown by the SR data. Subsequently, it became rainy and cloudy due
237 to the summer monsoon in the SCS. One notable meteorological feature during the campaign was the occurrence of the summer monsoon starting from May
238 27 close to the site *E*, during which (May 27–June 01), an increase of RH (~9% from campaign-averaged 78.7% to monsoon period-averaged 85.6%) and a
239 slight decrease of pressure (~0.2% from 1007.4 to 1005.4 hPa) were observed. Meanwhile, the wind directions were mainly southerly during this period and
240 later changed to southwest.

241 It should be noted that Typhoon 202103 (CHOI-WAN) travelled across B→D, resulting in a bulge in the middle of the cruise route to avoid the typhoon
242 during June 03–05, 2021. The typhoon track is available online with the last accessed date Mar. 25, 2023: [http://agora.ex.nii.ac.jp/digital-](http://agora.ex.nii.ac.jp/digital-typhoon/summary/wnp/s/202103.html.en)
243 [typhoon/summary/wnp/s/202103.html.en](http://agora.ex.nii.ac.jp/digital-typhoon/summary/wnp/s/202103.html.en). The typhoon was initiated at 02:00 local time on May 31 and dissipated at 14:00 on June 05, 2021 (Figure S5). It
244 passed over our cruise route from June 03 to June 05, 2021. While no significant increase of absolute wind speed was seen in Figure 2, a significant increase
245 of relative wind speed was shown in Figure S2, along with an obvious decrease of atmospheric pressure during the typhoon period (Figure S5). The measured
246 relative humidity increased from May 27 to June 01, prior to the presence of the typhoon, which can be attributed to the decrease of ambient temperature
247 during this period.

248 Figure 3 shows the time series of the mass concentrations of carbonaceous aerosol components in PM_{2.5} (i.e., BC, UVPM, OC, and EC) during the whole
249 campaign. Frequently high spikes of the mass concentrations of carbonaceous aerosol components were observed due to the ship pollution from the research
250 vessel. We notice that ship pollution was significantly pronounced on the first two days after the ship left the harbor and on the last 3–4 days before the ship
251 returned to the harbor, during which the spikes of BC and UVPM concentrations were measured by the Magee AE33 aethalometer with the relative wind
252 direction of 80–280°. Before May 08 and after June 05, higher UVPM, OC, and EC concentrations were observed, which can be attributed to significant fresh
253 ship emissions from the research vessel, as evidenced by simultaneous higher BC concentrations. Similar spikes in BC concentrations were observed during
254 other measurement periods, either preceding or following the monsoon period, which were caused by emissions from the frequent stops and starts of the ship.
255 Note that no significant diurnal trend for OC was observed during those aforementioned periods.

256 Figure 4 shows the time series of fire spots distribution and the 72-h backward trajectories at three AGLs (100, 500 and 1000 m) over the SCS during the
257 campaign. Only several backward trajectories are shown to avoid massive overlapping. Several fire spots located in the sea were attributed to oil or natural
258 gas drilling processes which generate thermal energy, combustion, and exhaust. Such processes included the prevalent hydrocarbon exploration and production
259 activities in this region. A comprehensive cartographic representation of these endeavors within the SCS can be accessed via the online platforms
260 (<https://amti.csis.org/south-china-sea-energy-exploration-and-development/>). Note that since the ship moved along the cruise route, the air mass backward
261 trajectories also changed with the movement of the ship. For example, significant biomass burning was detected in Laos, northern Vietnam, and the Philippines
262 during May 15–24, as indicated by the corresponding fire spots. However, the back trajectories to the sampling route (C→D) during this period were mainly
263 from the Philippines.

264 Here, we classified the campaign period into several groups based on the cruise route, change of wind direction during monsoon, backward trajectories,
265 and ship pollution, as listed in Table 1: (1) BMP-1 (before monsoon period 1), AB route mainly with northeast wind direction during May 05–09; (2) BMP-
266 2, B→C→D route close to the Philippines primarily with southeast wind direction during May 10–22; (3) BMP-3, D→E close to mainland China with the
267 same wind direction as BMP-2 during May 23–26; (4) TMP (transition monsoon period), EB route with south wind direction during May 27–Jun 01; (5) AMP
268 (after monsoon period), B→D→A route with southwest wind direction during June 02–09; (6) SPP (ship pollution period), ~35% of the online measurement
269 data could be attributed to this category in this study due to the interference from the research vessel own emissions.

270 3.2 Single particle analysis of BC and tar balls

271 Particle size distribution, composition, and size-dependent BC fractals were investigated based on TEM images. The Feret diameter is commonly used in

272 microscopy for particle size analysis (Zefirov et al., 2018). The size distribution of all the single particles from the analyzed TEM images is depicted in Fig.
273 5. The distribution is represented with histograms starting at 50 nm, a width interval of 20 nm, and a bin number of 200. The choice of bin width may vary
274 depending on cases but it is close to the quotient value of the square root of the measured particle number divided by the overall width of the distribution
275 (Pabst and Gregorova, 2007). Moreover, lognormal fitting is used for the peak size identification of particle size distribution (Rice et al., 2013). Figure 5a
276 shows a fitted peak Feret diameter of 307 nm for a total of 6613 particles from 15 samples during navigation, while a fitted peak Feret diameter of 325 nm
277 was obtained for a total of 9011 particles from 19 samples during stop (Fig. 5b). Note that we could not successfully obtain a bimodal or multi-peak fit for the
278 data of the stop cases using multi-peak fitting function in the Igor Pro software, as shown in Figure S6. Hence, we believe that single peak fitting best described
279 the distribution in our stop cases, as illustrated in Figure 5. Particles collected during navigation were predominantly aged at high wind speeds, while particles
280 during stop were mixed significantly with freshly emitted particles from the own ship and from other merchant ships or those from long-range transport,
281 possibly leading to the variation of the size distribution. Although the bimodal distribution was observed from particles in the indoor air, which was likely
282 caused by fresh emissions and secondary formation (Pipal et al., 2021), we did not obtain significant bimodal peaks for both navigation and stop particles.

283 We obtained characteristic values for the particle shape descriptors such as circularity (0.7 ± 0.2) and aspect ratio (1.2 ± 0.3) for all the particles collected
284 during navigation and stop, implying that these particles are not perfectly spherical and may vary in their mixing states. Figure 6 (top images) shows a
285 comparison of the mixing states during navigation (a-c) and stop (d-f) from typical BC TEM images. The BC particles collected during navigation are in the
286 embedded (a), external (b), or core-shell (c) mixing states classified with the methods which are based on single particle analysis of island and mountain
287 samples across East China Sea and Japan (Adachi et al., 2014; Sun et al., 2020a). More TEM images for the heavily coated internal and external BC particles
288 from navigation can be found in the SI (section 7, Fig. S7). The EDS analysis showed that the single particles during navigation were predominantly composed
289 of carbon (C), oxygen (O), sulfur (S), potassium (K), sodium (Na), chloride (Cl), magnesium (Mg), and calcium (Ca) (Fig. S8), indicating that those BC
290 particles were coated with sulfate, sea salt, and organics. Furthermore, small externally mixed BC particles can be transported over the sea and easily coated
291 during long-range transport. Under the TEM electron beam, these coated volatile components were easily vaporized to expose the BC fractal frame (Fig. S7d-
292 f).

293 Comparatively, a mixture of aged BC particles and much larger fresh BC particles as well as smaller scattered BC particles during stop were found (Fig.
294 6d-f), which were likely emitted from other ships (Fig. 6d) and the research vessel (e, f). These TEM images showed that the compressed BC particles are
295 typically more aged and atmospherically processed, while the fractal BC particles are fresh. Moreover, EDS analysis showed that sulfate formed from aqueous
296 processes and less viscous organic coating indicate an aging process. Those BC particles with Feret diameters larger than $2 \mu\text{m}$ during stop were fractal

297 agglomerates which could unlikely survive due to deposition during long-range transport. In addition, heavily coated internal BC particles were found during stop
298 due to the mixing between ship pollution and the marine air (Fig. S9). Moreover, such particles could also be condensation of organics during the cooling
299 process after they were emitted from the ship engine. The bottom panels of Fig. 6 (a-f) show the corresponding images obtained by boxing counting in fractal
300 analysis with the resultant D_f , Feret diameter (D), Lacunarity (L), and sampling number underneath for each TEM sample image. Figure 7 shows D_f and L as
301 a function of D for some representative BC particles during both navigation and stop. The BC particles showed narrower Feret diameters (229–2557 nm)
302 during navigation than those (78–2926 nm) of BC from the own ship during stop. The D_f values during navigation were in a range of 1.28–1.77 with a median
303 of 1.61, while the D_f values during stop were 1.43–1.76 with a median of 1.61, indicating no significant differences of D_f for the exposed BC particles during
304 navigation and stop. Note that the particles in Figure 7 include pure BC and BC without thick coatings. These particles were exposed to the electron beam and
305 volatile coatings were removed so that the morphology of BC was clearly shown regardless of the mixing state of the original BC particles (Figure S7). Most
306 BC particles were below 1 μm in Feret diameter during navigation (Figure 7), while their sizes cover a wide range below 3 μm during stop, implying that the
307 aged BC particles become smaller after long-range transport. Despite only a total of 134 BC data points shown in Figure 7, the results are still statistically
308 meaningful due to the wide range of BC sizes covered in our analysis. Note that the size change of a BC particle cannot be determined because the original
309 size of the particle is unknown before the removal of the coatings. Comparatively, the lacunarity during navigation (0.34–0.82, median: 0.53) and stop (0.34–
310 0.92, median: 0.59) were slightly different, with the former being smaller than the latter, indicating that the lacunarity tended to become smaller (~10%) after
311 coating or aging of the BC particles.

312 Tar balls were frequently observed during the campaign with an estimated sample fraction of about 11.8%. Fractal-like tar ball aggregates were usually
313 found in wildfire smokes (Grotto et al., 2018); however, in this study, spherical tar ball particles were observed in the marine atmosphere and were mixed
314 with sea salt (Fig. 8a and d for TEM image and EDS spectrum, respectively), organic carbon and sulfate (Fig. 8b and e) from the samples collected on May
315 27 during navigation. In contrast, the particles collected on June 01 were found to be amorphous carbon agglomerates (Fig. 8c and f) which were referred to
316 OC. During these days, the wind directions were from the southwest, with air masses originating from both the Philippines and Southeast Asia. The shape
317 difference between the tar ball spheres and the amorphous carbon agglomerates may be related to the type of biomass burning or the origin of the ship engines.
318 Similar particle morphologies were found in other studies on brown carbon during aircraft measurements over the Yellow Sea in 2001 (Zhu et al., 2013). Tar
319 balls mixed with BC during stop were also observed (Fig. S10), with geometrical diameters of 160–420 nm, much larger than nano-soot spheres (40–50 nm)
320 (Fig. S11). In comparison, the laboratory-generated tar balls were measured to have AAE values of 2.7–3.4, with an average of 2.9 at 467–652 nm (Hoffer et
321 al., 2016).

322 3.3 Light absorption of carbonaceous aerosols

323 The BC concentrations measured by the Magee AE33 aethalometer agree excellently with the optical EC concentrations obtained from the Sunset OC/EC
324 analyzer, as evidenced by a linear regression coefficient of 0.97. The BC measurements obtained from the AE33 instrument do not agree with the OC, EC
325 values, yet their overall trends exhibit consistency. However, the BC concentrations were considerably higher than the thermal EC concentrations, exhibiting
326 linear regression coefficients of 1.66 and 1.55, respectively. These findings, presented in Fig. S12 of Section 8 in the SI, are in line with previous research
327 conducted by Brown et al. (2019). The OC/EC ratios can be used as an indicator for the source origins of the air masses. Figure 9 shows the distribution of
328 the OC/EC ratios and the corresponding EC concentrations. The median OC/EC ratios are 8.14, 5.20, 6.35 and 2.63 for the classified periods BMP, TMP,
329 AMP, and SPP, respectively. Notably, EC median mass concentrations (0.24 , 0.25 and $0.17 \mu\text{g m}^{-3}$) for the marine air masses during BMP (0.013 – $0.69 \mu\text{g m}^{-3}$)
330 3), TMP (0.015 – $0.60 \mu\text{g m}^{-3}$), AMP (0.014 – $0.74 \mu\text{g m}^{-3}$) were lower than the median concentration ($1.70 \mu\text{g m}^{-3}$) during SPP. Compared with Figure 9d, the
331 scattered higher OC/EC ratios in Figure 9a/b/c are caused by the very low EC concentrations. The presence of extremely low EC concentrations, often falling
332 below or near the detection limit, can introduce discrepancies in the calculation of the OC/EC split, ultimately resulting in inaccurate EC concentrations (Bauer
333 et al., 2009). In addition, this study revealed a significant variation in EC concentrations during SPP, ranging from 0.15 to $22.8 \mu\text{g m}^{-3}$. Previous studies
334 showed that OC/EC ratio could be characterized by various sources, ranging from 1.37 – 1.71 for residential cookstoves, 1.63 – 2.23 for rural emissions, 1.05 –
335 1.24 for diesel exhaust, and 0.80 – 1.12 for urban environments (Khan et al., 2012). A low OC/EC ratio (<3) corresponded to the predominant contribution of
336 the primary OC in submicron particles reported in a previous study in the Southern Indian Ocean, Northern Indian Ocean and Bay of Bengal (Neusiß, 2002).
337 Here, the median OC/EC ratio of 2.63 during SPP is much higher than the characteristic values of diesel combustion, most likely because the sample air
338 during SPP is composed of marine air and the own ship exhaust. Our results are consistent with a recent study which showed that the diesel combustion from
339 ships accounted for 15% of BrC in the total light absorption at a coastal site in Shanghai during June–July, 2021 (Kang et al., 2022). In contrast, the OC/EC
340 ratios during other periods (i.e., BMP, TMP and AMP) were even much higher (5.20 – 8.13), indicating that the aerosols were highly aged during the long-
341 range transport of biomass burning aerosols. This is also consistent with our recent study in the SCS which showed that during monsoon periods in the summer
342 of 2019. The biomass burning organic aerosols became aged through atmospheric processes during transport (Sun et al., 2023).

343 The long-range biomass burning transport affects the air mass in the SCS. Figure 10 illustrates the wavelength-dependent mass concentration measured by
344 the AE33 aethalometer during the campaign, showing (a) an example of a ship plume, and (b, c) two significant biomass burning events during BMP (BB-1:
345 6:00–7:00 on May 15 and 15:00–22:00 on May 16) and during TMP (BB-2: 15:00 on May 30–00:00 on May 31). The ship plumes, predominantly emitted

346 from fossil fuel combustion, showed similar absorption at all seven wavelengths. In contrast, significant absorption at low wavelengths was detected during
347 the biomass burning events, a phenomenon also observed in other field measurements in urban cities and towns where air masses were susceptible to biomass
348 burning (Zhang et al., 2017). A comparison of the two methods for AAE calculation is presented in the SI (Section 4, Fig. S4). The fitting results demonstrate
349 that the AAE calculated for all wavelengths was lower than the AAE calculated for only 470 and 950 nm wavelengths. The fitting slope is 0.78, and the
350 determination coefficient (R^2) is 0.98, indicating a strong correlation between the two methods.

351 Figure 11 shows the hourly averaged AAE derived from all wavelengths as a function of the BC concentrations by AE33 aethalometer with the median
352 (range) AAE values of 1.14 (0.57–1.48), 1.02 (0.51–1.36), 1.08 (0.54–1.42), and 1.06 (0.65–1.37), respectively, for the classified periods (BMP, TMP, AMP,
353 and SPP), and the corresponding BC median (range) mass concentrations of 0.28 (0.033–1.17), 0.14 (0.042–2.86), 0.17 (0.055–1.08), and 3.01 (0.21–36.5)
354 $\mu\text{g m}^{-3}$, respectively. Like EC, ship pollution led to emissions of high BC concentrations, reaching as high as 36.5 $\mu\text{g m}^{-3}$. The median BC concentrations
355 decreased significantly during TMP and AMP, likely due to the increase of the RH which further increased the scavenging of the BC particles during navigation
356 as reported previously (Girach et al., 2014). Note that the biomass burning events were excluded from the above calculations and are further discussed below.

357 During the biomass burning events, the correlations of AAE with AE33 BC and Delta-C concentrations are respectively shown in Figs. 11 and 12,
358 characterized by very high median AAE values (1.85 and 1.86, respectively for BB-1 and BB-2) and BC concentrations (1.93 and 1.67 $\mu\text{g m}^{-3}$). The BC mass
359 concentration ranged from 1.45 to 3.62 $\mu\text{g m}^{-3}$ during biomass burning events based on light absorption at wavelength of 880 nm. The mass concentration in
360 Figure 10 corresponds to BC mass concentration obtained at each wavelength. We have emphasized that BC mass concentration in this study is equivalent
361 BC at individual wavelength. Notably, efficient light absorption of BrC in the range at 370–660 nm was observed during the biomass burning events, while
362 no significant wavelength-dependent BC concentrations were found during the own ship pollution (Fig. 10a). The AAE values below 1 in Figure 11 are not
363 noises, in some cases due to aerosols from fossil fuel (Ezani et al., 2021) and in other cases, they can be even lower than 0.5 when paired with wavelengths
364 of 470 and 660 nm (Laing et al., 2020). The higher AAE values imply much stronger absorption of non-BC light-absorbing particles (BrC) at shorter (UV-
365 vis) wavelengths, which mainly originated from the biomass burning emissions (Ponczek et al., 2022). Moreover, the median OC/EC ratios were 5.03 and
366 5.29 respectively for the two biomass burning events, even much higher than those for SPP (Fig. 9). The 72-h backward trajectories also showed that the BB-
367 1 air masses mainly originated from the Philippines while the BB-2 air masses were from the mainland Vietnam, both with high densities of fire spots (Fig.
368 4). The AAE values were also highly correlated with the Delta-C values with a determination coefficient (R^2) of 0.92 (Fig. 12), further demonstrating a
369 significant contribution of BrC to the AAE enhancement. In addition, we further correlated the observed high AAE values with the Delta-C values for the two
370 biomass burning events and confirmed that these high AAE values (1.45–3.62) were indeed attributed to biomass burning rather than ship emitted tar balls

371 which covered an AAE range of 2.7–3.7 at 405 and 781 nm wavelengths in a previous wood burning study (Chylek et al., 2019).

372 Our study found that the AAE values from all wavelengths for the marine atmosphere and ship pollution were 1.02–1.14 and 1.06, respectively, except for
373 a higher AAE value (1.93) during the two biomass burning events. The AAE values for ship pollution are dependent on the fuel types and loading conditions
374 (Laskin et al., 2015). For example, heavy fuel oil operated at high loads can result in AAE values (at 470/950 nm, and hereafter unless specified) of 2.0, while
375 the intermediate fuel oil has an AAE value of 1.3 at high loads (Helin et al., 2021). In addition, the presence of tar balls may contribute to the enhancement of
376 BrC absorption as mentioned in Section 3.2, as tar balls from ship emission have higher AAE values (2.5–6 depending on the wavelengths) (Corbin et al.,
377 2019). The occurrence of tar balls in this study was about 12% in the analyzed single samples. These tar balls were likely aged during long-range transport
378 from biomass burning and hence affected the light absorption of BrC in the SCS.

379 **3.4 BC sources from fossil fuel vs biomass burning**

380 The source origins of BC particles can be investigated using the AAE model. In the model, we employed respectively the characteristic AAE values of 1 and
381 2 for FF and BB to calculate their corresponding BC concentrations, namely BC(FF) and BC(BB). Figure 13 shows the time series of BC(FF) and BC(BB)
382 for different classified periods. The BC(FF) and BC(BB) values were much higher before the monsoon than during/after the monsoon, except for the periods
383 during BB-1 and BB-2 with significantly high BC(FF) and BC(BB) values (peaks $> 1 \mu\text{g m}^{-3}$), while high BC(FF) values were seen during SPP. Table 2
384 summarizes the average concentrations and the ranges of BC(FF) and BC(BB), along with their corresponding fractions. In general, both the average BC(FF)
385 and BC(BB) values were low during BMP, TMP, and AMP, compared to those during the biomass burning events and SPP. BC(FF) contributed over 80% of
386 ship pollution during SPP, whilst the BC(BB) could contribute to more than 40% of the total black carbon during the two BB events. We hence conclude that
387 fossil fuel combustion is the major contributor to the light absorption of BC except during the seasonal biomass burning events and biomass burning can have
388 a profound contribution to the BC light absorption in the SCS.

389 Active biomass burning pollution during January–May in Southeast Asia occurs routinely because of crop residue and sugar cane burning. A previous study
390 showed that during dry and wet seasons, the annual contribution of BC(BB) was 11% and 30% respectively in the Peninsular India (Soyam, 2021) based on
391 the two-component AAE model (Drinovec et al., 2015; Yus-Díez et al., 2021). Table 3 summarizes the BC concentrations, AAE values, and the corresponding
392 fraction of biomass burning (or fossil fuel) in previous and present studies for the marine atmosphere conducted at coastal sites or ship-based cruise
393 measurements using the AE series instrument. The BC(FF) and BC(BB) fractions of 58% and 42% were obtained respectively during the two BB events,
394 while they accounted for 78–83% and 18–22% during other periods, similar to those found at the coastal site in Central Adriatic (79% and 21%), and

395 significantly different from those reported at a coastal site in the East China Sea (Yu et al., 2018). However, observation data are still lacking on the contribution
396 of BC from fossil fuel vs biomass burning in the sea regions which warrants more future studies during different seasons.

397 **3.5 Limitation of this study**

398 This cruise campaign for carbonaceous aerosols has several limitations which might need to be aware of due to the time and area coverage constraints. The
399 presence of other light-absorption aerosol components, polluted dusts, oil and gas drilling emissions, as well as fishery policy may contribute to the
400 uncertainties in the AAE model used for the BC source apportionment in this study. Firstly, the composition of aerosols and refractive index may strongly
401 affect the AAE calculation. The source apportionment of BC for biomass burning and foil fuel is based on the AAE two-component model which only
402 considered BC(BB) and BC(FF) as the light absorption materials. An AAE range of 0.9–1.4 is used for pure BC from foil fuel emissions, while it is 1.68–2.2
403 for biomass burning as mentioned earlier. The current AAE two-component model does not include other potential light-absorbing materials, such as mineral
404 dust and biological particles (Pileci et al., 2021). Interestingly, two types of possible biological particles were observed during the campaign (Fig. S13, in the
405 SI, section 9). A similar type of biological particles was observed and identified as brocosomes in another campaign near the East China Sea (Fu et al., 2012).
406 However, more future studies are needed to identify the types and species of biological particles and to evaluate their contributions to the light-absorption.

407 Secondly, based on the Cloud-Aerosol Lidar & Infrared Satellite Observation (CALIPSO) data on May 15 and June 07 when the orbit just passed over the
408 SCS region and the Southeast Asia (Fig. S14 and S15, in the SI, section 10), we found the presence of polluted dust in the vertical profile over the Philippines,
409 Indonesia, Thailand and Malaysia. Long-range transport of dust may affect our measured AAE data. Thirdly, oil and natural gas drilling (Liu and Li, 2021) is
410 active in the SCS region and the distribution map is available online (<https://www.oilmap.xyz/>). These activities potentially contribute to the BC emissions
411 (Cordes et al., 2016), and these BC are similar to those of continental emitted BC from incomplete burning of oil or natural gas.

412 Lastly, Chinese fishery policy enacts fishing prohibition for about three and a half months every year in the SCS during summer which corresponds to
413 May 01–Aug 16 in the year of 2021 in 12°N within our campaign region. Therefore, the cruise measurements mainly captured ship emissions from the
414 commercial ships in the SCS whose routes are available online (<https://www.marinetraffic.com/en/ais/home/centerx:116.6/centery:20.5/zoom:4>). The average
415 BC mass concentrations ($\sim 0.2 \mu\text{g m}^{-3}$ for BC(FF) and $0.05\text{--}0.08 \mu\text{g m}^{-3}$ for BC(BB)) are only limited to data of about a month and the coverage area. Hence,
416 more future measurements covering more seasons and wider areas are needed to better understand the morphology and optical properties of the carbonaceous
417 aerosols in the SCS.

418 5. Conclusions

419 As important components of carbonaceous aerosols, BC and BrC in the marine atmosphere may exert significantly positive climatic radiative forcing through
420 light absorption on the regional and global scales. However, quantification of their absorption potential is tremendously challenging due to little knowledge
421 on the microphysical properties, such as morphology, particle size, and mixing state of BC or BrC in the marine region such as SCS. This ship-based study is
422 intended to investigate the morphological and optical properties of the BC particles in the SCS during summer using a combined online aethalometer, semi-
423 online OC/EC analyzer, and offline TEM/EDS analyses. The results showed that the lognormal fitted Feret diameter distribution of the single particles peaks
424 at 325 nm when the ship stopped, while it peaks at 307 nm when the ship navigated. This minor difference in the size distribution could be attributed to the
425 distinguishable air mass origins of the own ship emissions for the former and the mixed other ship emissions and long-range transport for the latter. Furthermore,
426 the Feret diameters of the single particles spread much more narrowly during navigation (229-2557 nm) than those of the freshly emitted particles during stop
427 (78-2926 nm). In addition, the two types of single particles have same median fractal dimension values (1.61) but different lacunarity values (0.53 vs 0.59),
428 indicating their different aging degrees. The aged BC particles are present in various mixing states (core-shell, embedded, external) with other aerosol
429 components after long-range transport. Interestingly, a fraction of single particles were identified as tar balls with geometrical diameters of 160–420 nm which
430 were primarily mixed with sea salt, organics, BC, and sulfate, and those tar balls were found to originate from either ship emissions or long-range transport
431 of biomass burning.

432 Since the marine atmosphere is mainly subject to the influence of biomass burning and fossil fuel combustion, a two-component (BB and FF) AAE model
433 was employed to evaluate the source contributions to the light absorption of the BC particles. The modelling results indicated that BB and FF contributed
434 respectively to 18–22% and 78–82% of all the BC light absorption except for a substantial percentage of 42% for BB (hence 58% for FF) during the two
435 observed significant biomass burning events. The results from trajectory calculations showed that biomass burning was predominantly from the Philippines
436 and South East Asia before and after the summer monsoon during the cruise campaign. However, this highly simplified two-component AAE model may have
437 substantial uncertainties in the evaluation of the source contributions when other sources of BC particles were present and those included dust, biological
438 materials, oil and gas drilling emissions during the measurements. Nevertheless, this study demonstrates that emissions from commercial ships and biomass
439 burning from Southeast Asia contribute to the enhanced light absorption of the BC particles in the SCS, especially during the crop harvest seasons before
440 monsoon, and the aged BC particles became more aggregated after long-range transport of air masses containing biomass burning emissions.

441 **Author contributions**

442 JZ, CZS, and SZZ planned the cruise campaign. CZS, YYZ, BLL, MG, and XS performed the measurements. CZS performed the data analysis and wrote the
443 original draft. CZS and DXC performed funding acquisition. JZ and SZZ performed funding acquisition and supervision. All authors reviewed and edited the
444 manuscript.

445 **Declaration of competing interest**

446 The authors declare no conflict of interest.

447 **Data availability**

448 Data for figures and tables, along with raw data from online measurements and offline analyses of this study are available from JZ via
449 zhaojun23@mail.sysu.edu.cn upon request. The supplementary data are available online at xxx.

450 **Acknowledgements**

451 We acknowledge supports from the Guangdong Basic and Applied Basic Research Foundation (Grant No. 2022A1515011864; 2021A1515011556), the
452 National Natural Science Foundation of China (NSFC) (Grant No. 42175115; 42205108), and Guangdong Major Project of Basic and Applied Basic Research
453 (Grant No. 2020B0301030004), the Science and Technology Program of Guangdong Province (Science and Technology Innovation Platform Category, no.
454 2019B121201002), Guangdong Province Key Laboratory for Climate Change and Natural Disaster Studies (Grant 2020B1212060025). This study was also
455 supported by the Southern Marine Science and Engineering Guangdong Laboratory (Zhuhai) through its South China Sea Monsoon Experiment Cruise (No.
456 SML2021SI1002). Additional support from the crew of the vessel “Tan Kah Kee” is greatly acknowledged.

457 **References**

458 Adachi, K., Zaizen, Y., Kajino, M., and Igarashi, Y.: Mixing state of regionally transported soot particles and the coating effect on their size and shape at a
459 mountain site in Japan, *J. Geophys. Res. Atmos.*, 119, 5386-5396, <https://doi.org/10.1002/2013jd020880>, 2014.
460 Adachi, K., Sedlacek, A. J., III, Kleinman, L., Springston, S. R., Wang, J., Chand, D., Hubbe, J. M., Shilling, J. E., Onasch, T. B., Kinase, T., Sakata, K.,
461 Takahashi, Y., and Buseck, P. R.: Spherical tarball particles form through rapid chemical and physical changes of organic matter in biomass-burning smoke,

462 Proc. Natl. Acad. Sci. U.S.A., 116, 19336-19341, <https://doi.org/10.1073/pnas.1900129116>, 2019.

463 Alroe, J., Cravigan, L. T., Miljevic, B., Johnson, G. R., Selleck, P., Humphries, R. S., Keywood, M. D., Chambers, S. D., Williams, A. G., and Ristovski, Z.
464 D.: Marine productivity and synoptic meteorology drive summer-time variability in Southern Ocean aerosols, *Atmos. Chem. Phys. Discuss.*,
465 <https://doi.org/10.5194/acp-2019-1081>, 2019.

466 Andreae, M. O. and Gelencsér, A.: Black carbon or brown carbon? The nature of light-absorbing carbonaceous aerosols, *Atmos. Chem. Phys.*, 6, 3131-3148,
467 <https://doi.org/10.5194/acp-6-3131-2006>, 2006.

468 Ausmeel, S., Eriksson, A., Ahlberg, E., Sporre, M. K., Spanne, M., and Kristensson, A.: Ship plumes in the Baltic Sea sulfur emission control area: Chemical
469 characterization and contribution to coastal aerosol concentrations, *Atmos. Chem. Phys.*, 20, 9135-9151, <https://doi.org/10.5194/acp-20-9135-2020>, 2020.

470 Bao, M., Zhang, Y., Cao, F., Lin, Y., Wang, Y., Liu, X., Zhang, W., Fan, M. Y., Xie, F., Cary, R. A., Dixon, J., and Zhou, L.: Highly time-resolved
471 characterization of carbonaceous aerosols using a two-wavelength Sunset thermal-optical carbon analyzer, *Atmos. Meas. Tech.*, 14, 4053-4068,
472 <https://doi.org/10.5194/amt-14-4053-2021>, 2021.

473 Bauer, J. J., Yu, X.-Y., Cary, R., Laulainen, N., and Berkowitz, C.: Characterization of the Sunset semi-continuous carbon aerosol analyzer, *J. Air Waste Manag.*
474 *Assoc.*, 59, 826-833, <https://doi.org/10.3155/1047-3289.59.7.826>, 2009.

475 Bencs, L., Horemans, B., Buczyńska, A. J., Deutsch, F., Degraeuwe, B., Van Poppel, M., and Van Grieken, R.: Seasonality of ship emission related atmospheric
476 pollution over coastal and open waters of the North Sea, *Atmos. Environ.: X.*, 7, <https://doi.org/10.1016/j.aeoa.2020.100077>, 2020.

477 Blanco-Donado, E. P.: Source identification and global implications of black carbon, *Geosci. Front.*, <https://doi.org/10.1016/j.gsf.2021.101149>, 2022.

478 Bond, T. C., Doherty, S. J., Fahey, D. W., Forster, P. M., Berntsen, T., DeAngelo, B. J., Flanner, M. G., Ghan, S., Kärcher, B., Koch, D., Kinne, S., Kondo, Y.,
479 Quinn, P. K., Sarofim, M. C., Schultz, M. G., Schulz, M., Venkataraman, C., Zhang, H., Zhang, S., Bellouin, N., Guttikunda, S. K., Hopke, P. K., Jacobson,
480 M. Z., Kaiser, J. W., Klimont, Z., Lohmann, U., Schwarz, J. P., Shindell, D., Storelvmo, T., Warren, S. G., and Zender, C. S.: Bounding the role of black
481 carbon in the climate system: A scientific assessment, *J. Geophys. Res. Atmos.*, 118, 5380-5552, <https://doi.org/10.1002/jgrd.50171>, 2013.

482 Brown, S., Minor, H., O'Brien, T., Hameed, Y., Feenstra, B., Kuebler, D., Wetherell, W., Day, R., Tun, R., Landis, E., and Rice, J.: Review of Sunset OC/EC
483 instrument measurements during the EPA's Sunset carbon evaluation project, *Atmosphere (Basel)*, 10, 287, <https://doi.org/10.3390/atmos10050287>, 2019.

484 Budhavant, K., Andersson, A., Holmstrand, H., Bikkina, P., Bikkina, S., Sathesh, S. K., and Gustafsson, Ö.: Enhanced light-absorption of black carbon in
485 rainwater compared with aerosols over the Northern Indian Ocean, *J. Geophys. Res. Atmos.*, 125, <https://doi.org/10.1029/2019jd031246>, 2020.

486 Cai, M., Liang, B., Sun, Q., Zhou, S., Chen, X., Yuan, B., Shao, M., Tan, H., and Zhao, J.: Effects of continental emissions on cloud condensation nuclei
487 (CCN) activity in the northern South China Sea during summertime 2018, *Atmos. Chem. Phys.*, 20, 9153-9167, <https://doi.org/10.5194/acp-20-9153-2020>,
488 2020.

489 Cappa, C. D., Onasch, T. B., Massoli, P., Worsnop, D. R., Bates, T. S., Cross, E. S., Davidovits, P., Hakala, J., Hayden, K. L., Jobson, B. T., Kolesar, K. R.,
490 Lack, D. A., Lerner, B. M., Li, S.-M., Mellon, D., Nuaaman, I., Olfert, J. S., Petäjä, T., Quinn, P. K., Song, C., Subramanian, R., Williams, E. J., and Zaveri,
491 R. A.: Radiative absorption enhancements due to the mixing state of atmospheric black carbon, *Science*, 337, 1078, <https://doi.org/10.1126/science.1223447>,
492 2012.

493 Chakrabarty, R. K., Moosmüller, H., Garro, M. A., Arnott, W. P., Walker, J., Susott, R. A., Babbitt, R. E., Wold, C. E., Lincoln, E. N., and Hao, W. M.:
494 Emissions from the laboratory combustion of wildland fuels: Particle morphology and size, *J. Geophys. Res.*, 111, <https://doi.org/10.1029/2005jd006659>,
495 2006.

496 Chaubey, J. P., Moorthy, K. K., Babu, S. S., and Gogoi, M. M.: Spatio-temporal variations in aerosol properties over the oceanic regions between coastal India
497 and Antarctica, *J. Atmos. Sol. Terr. Phys.*, 104, 18-28, <https://doi.org/10.1016/j.jastp.2013.08.004>, 2013.

498 Chen, D., Cui, H., Zhao, Y., Yin, L., Lu, Y., and Wang, Q.: A two-year study of carbonaceous aerosols in ambient PM_{2.5} at a regional background site for

499 western Yangtze River Delta, China, *Atmos. Res.*, 183, 351-361, <https://doi.org/https://doi.org/10.1016/j.atmosres.2016.09.004>, 2017.

500 Chen, X., Ye, C., Wang, Y., Wu, Z., Zhu, T., Zhang, F., Ding, X., Shi, Z., Zheng, Z., and Li, W.: Quantifying evolution of soot mixing state from transboundary
501 transport of biomass burning emissions, *iScience*, 26, 108125, [10.1016/j.isci.2023.108125](https://doi.org/10.1016/j.isci.2023.108125), 2023.

502 Cheng, Z., Sharma, N., Tseng, K. P., Kovarik, L., and China, S.: Direct observation and assessment of phase states of ambient and lab-generated sub-micron
503 particles upon humidification, *RSC Adv*, 11, 15264-15272, [10.1039/d1ra02530a](https://doi.org/10.1039/d1ra02530a), 2021.

504 China, S., Mazzoleni, C., Gorkowski, K., Aiken, A. C., and Dubey, M. K.: Morphology and mixing state of individual freshly emitted wildfire carbonaceous
505 particles, *Nat. Commun.*, 4, 2122, <https://doi.org/10.1038/ncomms3122>, 2013.

506 Chylek, P., Lee, J. E., Romonosky, D. E., Gallo, F., Lou, S., Shrivastava, M., Carrico, C. M., Aiken, A. C., and Dubey, M. K.: Mie scattering captures observed
507 optical properties of ambient biomass burning plumes assuming uniform black, brown, and organic carbon mixtures, *J. Geophys. Res. Atmos.*, 124, 11406-
508 11427, <https://doi.org/10.1029/2019jd031224>, 2019.

509 Corbin, J. C., Czech, H., Massabò, D., de Mongeot, F. B., Jakobi, G., Liu, F., Lobo, P., Mennucci, C., Mensah, A. A., Orasche, J., Pieber, S. M., Prévôt, A. S.
510 H., Stengel, B., Tay, L. L., Zanutta, M., Zimmermann, R., El Haddad, I., and Gysel, M.: Infrared-absorbing carbonaceous tar can dominate light absorption
511 by marine-engine exhaust, *npj Clim. Atmos. Sci.*, 2, <https://doi.org/10.1038/s41612-019-0069-5>, 2019.

512 Cordes, E. E., Jones, D. O. B., Schlacher, T. A., Amon, D. J., Bernardino, A. F., Brooke, S., Carney, R., DeLeo, D. M., Dunlop, K. M., Escobar-Briones, E.
513 G., Gates, A. R., Génio, L., Gobin, J., Henry, L.-A., Herrera, S., Hoyt, S., Joye, M., Kark, S., Mestre, N. C., Metaxas, A., Pfeifer, S., Sink, K., Sweetman,
514 A. K., and Witte, U.: Environmental impacts of the deep-water oil and gas industry: A review to guide management strategies, *Front. Environ. Sci.*, 4,
515 <https://doi.org/10.3389/fenvs.2016.00058>, 2016.

516 Dong, Z., Kang, S., Qin, D., Shao, Y., Ulbrich, S., and Qin, X.: Variability in individual particle structure and mixing states between the glacier-snowpack
517 and atmosphere in the northeastern Tibetan Plateau, *The Cryosphere*, 12, 3877-3890, [10.5194/tc-12-3877-2018](https://doi.org/10.5194/tc-12-3877-2018), 2018.

518 Drinovec, L., Močnik, G., Zotter, P., Prévôt, A. S. H., Ruckstuhl, C., Coz, E., Rupakheti, M., Sciare, J., Müller, T., Wiedensohler, A., and Hansen, A. D. A.:
519 The "dual-spot" Aethalometer: An improved measurement of aerosol black carbon with real-time loading compensation, *Atmos. Meas. Tech.*, 8, 1965-1979,
520 <https://doi.org/10.5194/amt-8-1965-2015>, 2015.

521 Duarte, R. M. B. O., Gomes, J. F. P., Querol, X., Cattaneo, A., Bergmans, B., Saraga, D., Maggos, T., Di Gilio, A., Rovelli, S., and Villanueva, F.: Advanced
522 instrumental approaches for chemical characterization of indoor particulate matter, *Appl. Spectrosc. Rev.*, 57, 705-745,
523 <https://doi.org/10.1080/05704928.2021.2018596>, 2021.

524 Ezani, E., Dhandapani, S., Heal, M. R., Praveena, S. M., Khan, M. F., and Ramly, Z. T. A.: Characteristics and source apportionment of black carbon (BC) in
525 a suburban area of Klang Valley, Malaysia, *Atmosphere*, 12, <https://doi.org/10.3390/atmos12060784>, 2021.

526 Feng, X., Wang, J., Teng, S., Xu, X., Zhu, B., Wang, J., Zhu, X., Yurkin, M. A., and Liu, C.: Can light absorption of black carbon still be enhanced by mixing
527 with absorbing materials?, *Atmos. Environ.*, 253, 118358, <https://doi.org/10.1016/j.atmosenv.2021.118358>, 2021.

528 Fossum, K. N., Ovadnevaite, J., Liu, D., Flynn, M., O'Dowd, C., and Ceburnis, D.: Background levels of black carbon over remote marine locations, *Atmos.*
529 *Res.*, 271, <https://doi.org/10.1016/j.atmosres.2022.106119>, 2022.

530 Fu, H., Zhang, M., Li, W., Chen, J., Wang, L., Quan, X., and Wang, W.: Morphology, composition and mixing state of individual carbonaceous aerosol in
531 urban Shanghai, *Atmos. Chem. Phys.*, 12, 693-707, <https://doi.org/10.5194/acp-12-693-2012>, 2012.

532 Geron, C.: Carbonaceous aerosol over a Pinus taeda forest in Central North Carolina, USA, *Atmos. Environ.*, 43, 959-969,
533 <https://doi.org/10.1016/j.atmosenv.2008.10.053>, 2009.

534 Giglio, L., Schroeder, W., Hall, J. V., and Justice, C. O.: MODIS collection 6 active fire product user's guide revision C, University of Maryland. National
535 Oceanic and Atmospheric Administration, 63 pp., 2020.

536 Girach, I. A., Nair, V. S., Babu, S. S., and Nair, P. R.: Black carbon and carbon monoxide over Bay of Bengal during W_ICARB: Source characteristics, *Atmos.*
537 *Environ.*, 94, 508-517, <https://doi.org/10.1016/j.atmosenv.2014.05.054>, 2014.

538 Giroto, G., China, S., Bhandari, J., Gorkowski, K., Scarnato, B. V., Capek, T., Marinoni, A., Veghte, D. P., Kulkarni, G., Aiken, A. C., Dubey, M., and
539 Mazzoleni, C.: Fractal-like tar ball aggregates from wildfire smoke, *Environ. Sci. Technol. Lett.*, 5, 360-365, 10.1021/acs.estlett.8b00229, 2018. Hand, J.
540 L., Malm, W. C., Laskin, A., Day, D., Lee, T., Wang, C., Carrico, C., Carrillo, J., Cowin, J. P., Collett, J., and Iedema, M. J.: Optical, physical, and chemical
541 properties of tar balls observed during the Yosemite Aerosol Characterization Study, *J. Geophys. Res.*, 110, <https://doi.org/10.1029/2004jd005728>, 2005.

542 Harrison, R. M.: Airborne particulate matter, *Philos. Trans. R. Soc. A*, 378, 20190319, <https://doi.org/10.1098/rsta.2019.0319>, 2020.

543 Helin, A., Virkkula, A., Backman, J., Pirjola, L., Sippula, O., Aakko-Saksa, P., Väätäinen, S., Mylläri, F., Järvinen, A., Bloss, M., Aurela, M., Jakobi, G.,
544 Karjalainen, P., Zimmermann, R., Jokiniemi, J., Saarikoski, S., Tissari, J., Rönkkö, T., Niemi, J. V., and Timonen, H.: Variation of absorption Ångström
545 exponent in aerosols from different emission sources, *J. Geophys. Res. Atmos.*, 126, <https://doi.org/10.1029/2020jd034094>, 2021.

546 Hoffer, A., Tóth, A., Nyirő-Kósa, I., Pósfai, M., and Gelencsér, A.: Light absorption properties of laboratory-generated tar ball particles, *Atmos. Chem. Phys.*,
547 16, 239-246, <https://doi.org/10.5194/acp-16-239-2016>, 2016.

548 Jung, J., Kim, Y. J., Lee, K. Y., Kawamura, K., Hu, M., and Kondo, Y.: The effects of accumulated refractory particles and the peak inert mode temperature
549 on semi-continuous organic carbon and elemental carbon measurements during the CAREBeijing 2006 campaign, *Atmos. Environ.*, 45, 7192-7200,
550 <https://doi.org/10.1016/j.atmosenv.2011.09.003>, 2011.

551 Kang, H., Shang, X., Abdumutallip, M., Chen, Y., Li, L., Wang, X., Li, C., Ouyang, H., Tang, X., Wang, L., Rudich, Y., and Chen, J.: Accurate observation of
552 black and brown carbon in atmospheric fine particles via a versatile aerosol concentration enrichment system (VACES), *Sci. Total Environ.*, 837, 155817,
553 <https://doi.org/10.1016/j.scitotenv.2022.155817>, 2022.

554 Karanasiou, A., Panteliadis, P., Perez, N., Minguillon, M. C., Pandolfi, M., Titos, G., Viana, M., Moreno, T., Querol, X., and Alastuey, A.: Evaluation of the
555 Semi-Continuous OCEC analyzer performance with the EUSAAR2 protocol, *Sci. Total Environ.*, 747, 141266,
556 <https://doi.org/10.1016/j.scitotenv.2020.141266>, 2020.

557 Kedia, S., Ramachandran, S., Rajesh, T. A., and Srivastava, R.: Aerosol absorption over Bay of Bengal during winter: Variability and sources, *Atmos. Environ.*,
558 54, 738-745, <https://doi.org/10.1016/j.atmosenv.2011.12.047>, 2012.

559 Khan, B., Hays, M. D., Geron, C., and Jetter, J.: Differences in the OC/EC ratios that characterize ambient and source aerosols due to thermal-optical analysis,
560 *Aerosol Sci. Technol.*, 46, 127-137, <https://doi.org/10.1080/02786826.2011.609194>, 2012.

561 Kompalli, S. K., Babu, S. N. S., Moorthy, K. K., Satheesh, S. K., Gogoi, M. M., Nair, V. S., Jayachandran, V. N., Liu, D., Flynn, M. J., and Coe, H.: Mixing
562 state of refractory black carbon aerosol in the South Asian outflow over the northern Indian Ocean during winter, *Atmos. Chem. Phys.*, 21, 9173-9199,
563 <https://doi.org/10.5194/acp-21-9173-2021>, 2021.

564 Kwak, N., Lee, H., Maeng, H., Seo, A., Lee, K., Kim, S., Lee, M., Cha, J. W., Shin, B., and Park, K.: Morphological and chemical classification of fine
565 particles over the Yellow Sea during spring, 2015-2018, *Environ. Pollut.*, 305, 119286, <https://doi.org/10.1016/j.envpol.2022.119286>, 2022.

566 Lack, D. A. and Cappa, C. D.: Impact of brown and clear carbon on light absorption enhancement, single scatter albedo and absorption wavelength dependence
567 of black carbon, *Atmos. Chem. Phys.*, 10, 4207-4220, 10.5194/acp-10-4207-2010, 2010.

568 Laing, J. R., Jaffe, D. A., and Sedlacek, I. I. A. J.: Comparison of Filter-based Absorption Measurements of Biomass Burning Aerosol and Background
569 Aerosol at the Mt. Bachelor Observatory, *Aerosol Air Qual. Res.*, 20, 663-678, 10.4209/aaqr.2019.06.0298, 2020.

570 Lappi, M. K. and Ristimäki, J. M.: Evaluation of thermal optical analysis method of elemental carbon for marine fuel exhaust, *J. Air Waste Manag. Assoc.*,
571 67, 1298-1318, <https://doi.org/10.1080/10962247.2017.1335251>, 2017.

572 Laskin, A., Laskin, J., and Nizkorodov, S. A.: Chemistry of atmospheric brown carbon, *Chem. Rev.*, 115, 4335-4382, <https://doi.org/10.1021/cr5006167>, 2015.

573 Li, J., Zhang, Q., Wang, G., Li, J., Wu, C., Liu, L., Wang, J., Jiang, W., Li, L., Ho, K. F., and Cao, J.: Optical properties and molecular compositions of water-
574 soluble and water-insoluble brown carbon (BrC) aerosols in northwest China, *Atmos. Chem. Phys.*, 20, 4889-4904, [https://doi.org/10.5194/acp-20-4889-](https://doi.org/10.5194/acp-20-4889-2020)
575 [2020](https://doi.org/10.5194/acp-20-4889-2020), 2020.

576 Liu, J. and Li, X.: Recent advances on natural gas hydrate exploration and development in the South China Sea, *Energy Fuels*, 35, 7528-7552,
577 <https://doi.org/10.1021/acs.energyfuels.1c00494>, 2021.

578 Liu, L., Zhang, J., Zhang, Y., Wang, Y., Xu, L., Yuan, Q., Liu, D., Sun, Y., Fu, P., Shi, Z., and Li, W.: Persistent residential burning-related primary organic
579 particles during wintertime hazes in North China: insights into their aging and optical changes, *Atmos. Chem. Phys.*, 21, 2251-2265,
580 <https://doi.org/10.5194/acp-21-2251-2021>, 2021.

581 Liu, X., Zhu, R., Jin, B., Zu, L., Wang, Y., Wei, Y., and Zhang, R.: Emission characteristics and light absorption apportionment of carbonaceous aerosols: A
582 tunnel test conducted in an urban with fully enclosed use of E10 petrol, *Environ. Res.*, 216, <https://doi.org/10.1016/j.envres.2022.114701>, 2023.

583 Lu, Q., Liu, C., Zhao, D., Zeng, C., Li, J., Lu, C., Wang, J., and Zhu, B.: Atmospheric heating rate due to black carbon aerosols: Uncertainties and impact
584 factors, *Atmos. Res.*, 240, <https://doi.org/10.1016/j.atmosres.2020.104891>, 2020.

585 Luo, J., Zhang, Y., and Zhang, Q.: Effects of black carbon morphology on brown carbon absorption estimation: From numerical aspects, *Geosci. Model Dev.*,
586 14, 2113-2126, <https://doi.org/10.5194/gmd-14-2113-2021>, 2021.

587 Luo, J., Li, Z., Zhang, C., Zhang, Q., Zhang, Y., Zhang, Y., Curci, G., and Chakrabarty, R. K.: Regional impacts of black carbon morphologies on shortwave
588 aerosol-radiation interactions: A comparative study between the US and China, *Atmos. Chem. Phys.*, 22, 7647-7666, [https://doi.org/10.5194/acp-22-7647-](https://doi.org/10.5194/acp-22-7647-2022)
589 [2022](https://doi.org/10.5194/acp-22-7647-2022), 2022.

590 Ma, Y., Zhang, X., Xin, J., Zhang, W., Wang, Z., Liu, Q., Wu, F., Wang, L., Lyu, Y., Wang, Q., and Ma, Y.: Mass and number concentration distribution of
591 marine aerosol in the Western Pacific and the influence of continental transport, *Environ. Pollut.*, 298, 118827, <https://doi.org/10.1016/j.envpol.2022.118827>,
592 2022.

593 Marple, V. A. and Olson, B. A.: Sampling and measurement using inertial, gravitational, centrifugal, and thermal techniques, in: *Aerosol measurement: Principles, techniques, and applications*, edited by: Kulkarni, P., Baron, P. A., and Willeke, K., John Wiley and Sons, Hoboken, New Jersey, USA, 129-151,
594 <https://doi.org/10.1002/9781118001684.ch8>, 2011.

596 Matsui, H., Koike, M., Kondo, Y., Oshima, N., Moteki, N., Kanaya, Y., Takami, A., and Irwin, M.: Seasonal variations of Asian black carbon outflow to the
597 Pacific: Contribution from anthropogenic sources in China and biomass burning sources in Siberia and Southeast Asia, *J. Geophys. Res. Atmos.*, 118, 9948-
598 9967, <https://doi.org/10.1002/jgrd.50702>, 2013.

599 Milinković, A., Gregorič, A., Grgičin, V. D., Vidič, S., Penezić, A., Kušan, A. C., Alempijević, S. B., Kasper-Giebl, A., and Frka, S.: Variability of black carbon
600 aerosol concentrations and sources at a Mediterranean coastal region, *Atmos. Pollut. Res.*, 12, <https://doi.org/10.1016/j.apr.2021.101221>, 2021.

601 Moschos, V., Gysel-Beer, M., Modini, R. L., Corbin, J. C., Massabò, D., Costa, C., Danelli, S. G., Vlachou, A., Daellenbach, K. R., Szidat, S., Prati, P., Prévôt,
602 A. S. H., Baltensperger, U., and El Haddad, I.: Source-specific light absorption by carbonaceous components in the complex aerosol matrix from yearly
603 filter-based measurements, *Atmos. Chem. Phys.*, 21, 12809-12833, <https://doi.org/10.5194/acp-21-12809-2021>, 2021.

604 Neustüß, C.: Carbonaceous aerosol over the Indian Ocean: OC/EC fractions and selected specifications from size-segregated onboard samples, *J. Geophys. Res.*, 107,
605 <https://doi.org/10.1029/2001jd000327>, 2002.

606 Pabst, W. and Gregorova, E.: Characterization of particles and particle systems, *ICT Prague*, 122, 122, 2007.

607 Pang, Y., Wang, Y., Wang, Z., Zhang, Y., Liu, L., Kong, S., Liu, F., Shi, Z., and Li, W.: Quantifying the fractal dimension and morphology of individual
608 atmospheric soot aggregates, *J. Geophys. Res. Atmos.*, 127, <https://doi.org/10.1029/2021jd036055>, 2022.

609 Pankratova, N. V., Belikov, I. B., Belousov, V. A., Kopeikin, V. M., Skorokhod, A. I., Shtabkin, Y. A., Malafeev, G. V., and Flint, M. V.: Concentration and

610 isotopic composition of methane, associated gases, and black carbon over Russian Arctic Seas (shipborne measurements), *Oceanology*, 60, 593-602,
611 <https://doi.org/10.1134/s0001437020050197>, 2021.

612 Park, S., Yu, G.-H., and Lee, S.: Optical absorption characteristics of brown carbon aerosols during the KORUS-AQ campaign at an urban site, *Atmos. Res.*,
613 203, 16-27, <https://doi.org/10.1016/j.atmosres.2017.12.002>, 2018.

614 Peyronel, M. F., Acevedo, N. C., and Marangoni, A. G.: Structural and mechanical properties of fats and their implications for food quality, in: *Chemical*
615 *deterioration and physical instability of food and beverages*, edited by: Skibsted, L. H., Risbo, J., and Andersen, M. L., Woodhead Publishing Limited,
616 Abington Hall, Granta Park, Great Abington, Cambridge CB21 6AH, UK, 216-259, <https://doi.org/10.1533/9781845699260.2.216>, 2010.

617 Pileci, R. E., Modini, R. L., Bertò, M., Yuan, J., Corbin, J. C., Marinoni, A., Henzing, B., Moerman, M. M., Putaud, J. P., Spindler, G., Wehner, B., Müller, T.,
618 Tuch, T., Trentini, A., Zanatta, M., Baltensperger, U., and Gysel-Beer, M.: Comparison of co-located refractory black carbon (rBC) and elemental carbon
619 (EC) mass concentration measurements during field campaigns at several European sites, *Atmos. Meas. Tech.*, 14, 1379-1403, [https://doi.org/10.5194/amt-](https://doi.org/10.5194/amt-14-1379-2021)
620 [14-1379-2021](https://doi.org/10.5194/amt-14-1379-2021), 2021.

621 Pipal, A. S., Rohra, H., Tiwari, R., and Taneja, A.: Particle size distribution, morphometric study and mixing structure of accumulation and ultrafine aerosols
622 emitted from indoor activities in different socioeconomic micro-environment, *Atmos. Pollut. Res.*, 12, 101-111, <https://doi.org/10.1016/j.apr.2021.02.015>,
623 2021.

624 Ponczek, M., Franco, M. A., Carbone, S., Rizzo, L. V., Monteiro dos Santos, D., Morais, F. G., Duarte, A., Barbosa, H. M. J., and Artaxo, P.: Linking the
625 chemical composition and optical properties of biomass burning aerosols in Amazonia, *Environ. Sci. Atmos.*, 2, 252-269,
626 <https://doi.org/10.1039/d1ea00055a>, 2022.

627 Rabha, S. and Saikia, B. K.: An environmental evaluation of carbonaceous aerosols in PM10 at micro- and nano-scale levels reveals the formation of carbon
628 nanodots, *Chemosphere*, 244, 125519, <https://doi.org/10.1016/j.chemosphere.2019.125519>, 2020.

629 Retama, A., Ramos-Cerón, M., Rivera-Hernández, O., Allen, G., and Velasco, E.: Aerosol optical properties and brown carbon in Mexico City, *Environ. Sci.*
630 *Atmos.*, 2, 315-334, <https://doi.org/10.1039/d2ea00006g>, 2022.

631 Rice, S. B., Chan, C., Brown, S. C., Eschbach, P., Han, L., Ensor, D. S., Stefaniak, A. B., Bonevich, J., Vladar, A. E., Hight Walker, A. R., Zheng, J., Starnes,
632 C., Stromberg, A., Ye, J., and Grulke, E. A.: Particle size distributions by transmission electron microscopy: An interlaboratory comparison case study,
633 *Metrologia*, 50, 663-678, <https://doi.org/10.1088/0026-1394/50/6/663>, 2013.

634 Schmale, J., Baccarini, A., Thurnherr, I., Henning, S., Efraim, A., Regayre, L., Bolas, C., Hartmann, M., Welti, A., Lehtipalo, K., Aemisegger, F., Tatzelt, C.,
635 Landwehr, S., Modini, R. L., Tummon, F., Johnson, J. S., Harris, N., Schnaiter, M., Toffoli, A., Derkani, M., Bukowiecki, N., Stratmann, F., Dommen, J.,
636 Baltensperger, U., Wernli, H., Rosenfeld, D., Gysel-Beer, M., and Carslaw, K. S.: Overview of the Antarctic Circumnavigation Expedition: Study of
637 Preindustrial-like aerosols and their climate effects (ACE-SPACE), *Bull. Am. Meteorol. Soc.*, 100, 2260-2283, <https://doi.org/10.1175/bams-d-18-0187.1>,
638 2019.

639 Shamjad, P. M., Tripathi, S. N., Aggarwal, S. G., Mishra, S. K., Joshi, M., Khan, A., Sapra, B. K., and Ram, K.: Comparison of experimental and modeled
640 absorption enhancement by black carbon (BC) cored polydisperse aerosols under hygroscopic conditions, *Environ. Sci. Technol.*, 46, 8082-8089,
641 <https://doi.org/10.1021/es300295y>, 2012.

642 Shank, L. M., Howell, S., Clarke, A. D., Freitag, S., Brekhovskikh, V., Kapustin, V., McNaughton, C., Campos, T., and Wood, R.: Organic matter and non-
643 refractory aerosol over the remote Southeast Pacific: Oceanic and combustion sources, *Atmos. Chem. Phys.*, 12, 557-576, [https://doi.org/10.5194/acp-12-](https://doi.org/10.5194/acp-12-557-2012)
644 [557-2012](https://doi.org/10.5194/acp-12-557-2012), 2012.

645 Sharma, S., Barrie, L. A., Magnusson, E., Brattström, G., Leaitch, W. R., Steffen, A., and Landsberger, S.: A factor and trends analysis of multidecadal lower
646 tropospheric observations of Arctic aerosol composition, black carbon, ozone, and mercury at Alert, Canada, *J. Geophys. Res. Atmos.*, 124, 14133-14161,

647 <https://doi.org/10.1029/2019jd030844>, 2019.

648 Song, X., Xie, X., Qiu, B., Cao, H., Xie, S.-P., Chen, Z., and Yu, W.: Air-sea latent heat flux anomalies induced by oceanic submesoscale processes: An
649 observational case study, *Front. Mar. Sci.*, 9, 10.3389/fmars.2022.850207, 2022.

650 Soyam, P. S.: Black carbon aerosols over a semi-arid rain shadow location in Peninsular India: Temporal variability and sources, *J. Earth Syst. Sci.*, 130,
651 <https://doi.org/10.1007/s12040-021-01610-5>, 2021.

652 Sun, C., Adachi, K., Misawa, K., Cheung, H. C., Chou, C. C. K., and Takegawa, N.: Mixing state of black carbon particles in Asian outflow observed at a
653 remote site in Taiwan in the spring of 2017, *J. Geophys. Res. Atmos.*, 125, 13, <https://doi.org/10.1029/2020jd032526>, 2020a.

654 Sun, L., Chen, T., Jiang, Y., Zhou, Y., Sheng, L., Lin, J., Li, J., Dong, C., Wang, C., Wang, X., Zhang, Q., Wang, W., and Xue, L.: Ship emission of nitrous
655 acid (HONO) and its impacts on the marine atmospheric oxidation chemistry, *Sci. Total Environ.*, 735, 139355,
656 <https://doi.org/10.1016/j.scitotenv.2020.139355>, 2020b.

657 Sun, Q., Liang, B., Cai, M., Zhang, Y., Ou, H., Ni, X., Sun, X., Han, B., Deng, X., Zhou, S., and Zhao, J.: Cruise observation of the marine atmosphere and
658 ship emissions in South China Sea: Aerosol composition, sources, and the aging process, *Environ. Pollut.*, 316, 120539,
659 <https://doi.org/10.1016/j.envpol.2022.120539>, 2023.

660 Sun, T., Wu, C., Wu, D., Liu, B., Sun, J. Y., Mao, X., Yang, H., Deng, T., Song, L., Li, M., Li, Y. J., and Zhou, Z.: Time-resolved black carbon aerosol vertical
661 distribution measurements using a 356-m meteorological tower in Shenzhen, *Theor. Appl. Climatol.*, 140, 1263-1276, <https://doi.org/10.1007/s00704-020-03168-6>, 2020c.

662

663 Taketani, F., Miyakawa, T., Takashima, H., Komazaki, Y., Pan, X., Kanaya, Y., and Inoue, J.: Shipborne observations of atmospheric black carbon aerosol
664 particles over the Arctic Ocean, Bering Sea, and North Pacific Ocean during September 2014, *J. Geophys. Res. Atmos.*, 121, 1914-1921,
665 <https://doi.org/10.1002/2015jd023648>, 2016.

666 Tóth, A., Hoffer, A., Nyirő-Kósa, I., Pósfai, M., and Gelencsér, A.: Atmospheric tar balls: aged primary droplets from biomass burning?, *Atmos. Chem. Phys.*,
667 14, 6669-6675, <https://doi.org/10.5194/acp-14-6669-2014>, 2014.

668 Ueda, S., Osada, K., Hara, K., Yabuki, M., Hashihama, F., and Kanda, J.: Morphological features and mixing states of soot-containing particles in the marine
669 boundary layer over the Indian and Southern oceans, *Atmos. Chem. Phys.*, 18, 9207-9224, <https://doi.org/10.5194/acp-18-9207-2018>, 2018.

670 Virkkula, A.: Modeled source apportionment of black carbon particles coated with a light-scattering shell, *Atmos. Meas. Tech.*, 14, 3707-3719,
671 <https://doi.org/10.5194/amt-14-3707-2021>, 2021.

672 Wang, G., Chen, J., Xu, J., Yun, L., Zhang, M., Li, H., Qin, X., Deng, C., Zheng, H., Gui, H., Liu, J., and Huang, K.: Atmospheric processing at the sea-land
673 interface over the South China Sea: Secondary aerosol formation, aerosol acidity, and role of sea salts, *J. Geophys. Res. Atmos.*, 127,
674 <https://doi.org/10.1029/2021jd036255>, 2022.

675 Wang, Q., Liu, H., Ye, J., Tian, J., Zhang, T., Zhang, Y., Liu, S., and Cao, J.: Estimating absorption Ångström exponent of black carbon aerosol by coupling
676 multiwavelength absorption with chemical composition, *Environ. Sci. Technol.*, 8, 121-127, <https://doi.org/10.1021/acs.estlett.0c00829>, 2020a.

677 Wang, Q., Liu, H., Wang, P., Dai, W., Zhang, T., Zhao, Y., Tian, J., Zhang, W., Han, Y., and Cao, J.: Optical source apportionment and radiative effect of light-
678 absorbing carbonaceous aerosols in a tropical marine monsoon climate zone: The importance of ship emissions, *Atmos. Chem. Phys.*, 20, 15537-15549,
679 <https://doi.org/10.5194/acp-20-15537-2020>, 2020b.

680 Wang, Y., Liu, F., He, C., Bi, L., Cheng, T., Wang, Z., Zhang, H., Zhang, X., Shi, Z., and Li, W.: Fractal dimensions and mixing structures of soot particles
681 during atmospheric processing, *Environ. Sci. Technol.*, 4, 487-493, <https://doi.org/10.1021/acs.estlett.7b00418>, 2017.

682 Wang, Y. L. and Wu, C. R.: Nonstationary El Niño teleconnection on the post-summer upwelling off Vietnam, *Sci. Rep.*, 10, 13319,
683 <https://doi.org/10.1038/s41598-020-70147-2>, 2020.

684 Wei, X., Zhu, Y., Hu, J., Liu, C., Ge, X., Guo, S., Liu, D., Liao, H., and Wang, H.: Recent progress in impacts of mixing state on optical properties of black
685 carbon aerosol, *Curr. Pollut. Rep.*, 6, 380-398, <https://doi.org/10.1007/s40726-020-00158-0>, 2020.

686 Wu, D., Wu, C., Liao, B., Chen, H., Wu, M., Li, F., Tan, H., Deng, T., Li, H., Jiang, D., and Yu, J. Z.: Black carbon over the South China Sea and in various
687 continental locations in South China, *Atmos. Chem. Phys.*, 13, 12257-12270, <https://doi.org/10.5194/acp-13-12257-2013>, 2013a.

688 Wu, H., Lattuada, M., and Morbidelli, M.: Dependence of fractal dimension of DLCA clusters on size of primary particles, *Adv. Colloid Interface Sci.*, 195-
689 196, 41-49, <https://doi.org/10.1016/j.cis.2013.04.001>, 2013b.

690 Xing, J., Bian, L., Hu, Q., Yu, J., Sun, C., and Xie, Z.: Atmospheric black carbon along a cruise path through the Arctic Ocean during the fifth Chinese Arctic
691 Research Expedition, *Atmosphere*, 5, 292-306, <https://doi.org/10.3390/atmos5020292>, 2014.

692 Yan, J., Chen, L., Zhao, S., Zhang, M., Lin, Q., and Li, L.: Impact of marine and continental sources on aerosol characteristics using an on-board SPAMS over
693 southeast sea, China, *Environ. Sci. Pollut. Res.*, 25, 30659-30670, <https://doi.org/10.1007/s11356-018-2902-5>, 2018.

694 Yang, M., Howell, S. G., Zhuang, J., and Huebert, B. J.: Attribution of aerosol light absorption to black carbon, brown carbon, and dust in China –
695 interpretations of atmospheric measurements during EAST-AIRE, *Atmos. Chem. Phys.*, 9, 2035-2050, <https://doi.org/10.5194/acp-9-2035-2009>, 2009.

696 You, R., Radney, J. G., Zachariah, M. R., and Zangmeister, C. D.: Measured wavelength-dependent absorption enhancement of internally mixed black carbon
697 with absorbing and nonabsorbing materials, *Environ. Sci. Technol.*, 50, 7982-7990, <https://doi.org/10.1021/acs.est.6b01473>, 2016.

698 Yu, G.-H., Park, S., Shin, S.-K., Lee, K.-H., and Nam, H.-G.: Enhanced light absorption due to aerosol particles in ship plumes observed at a seashore site,
699 *Atmos. Pollut. Res.*, 9, 1177-1183, <https://doi.org/10.1016/j.apr.2018.05.005>, 2018.

700 Yus-Díez, J., Bernardoni, V., Močnik, G., Alastuey, A., Ciniglia, D., Ivančič, M., Querol, X., Perez, N., Reche, C., Rigler, M., Vecchi, R., Valentini, S., and
701 Pandolfi, M.: Determination of the multiple-scattering correction factor and its cross-sensitivity to scattering and wavelength dependence for different AE33
702 Aethalometer filter tapes: A multi-instrumental approach, *Atmos. Meas. Tech.*, 14, 6335-6355, <https://doi.org/10.5194/amt-14-6335-2021>, 2021.

703 Zefirov, V. V., Elmanovich, I. V., Levin, E. E., Abramchuk, S. S., Kharitonova, E. P., Khokhlov, A. A., Kondratenko, M. S., and Gallyamov, M. O.: Synthesis
704 of manganese oxide electrocatalysts in supercritical carbon dioxide, *J. Mater. Sci.*, 53, 9449-9462, <https://doi.org/10.1007/s10853-018-2242-3>, 2018.

705 Zhang, K., Allen, G., Yang, B., Chen, G., Gu, J., Schwab, J. J., Felton, D., and Rattigan, O.: Joint measurements of PM_{2.5} and light-absorptive PM in
706 woodsmoke-dominated ambient and plume environments, *Atmos. Chem. Phys.*, 17, 11441-11452, <https://doi.org/10.5194/acp-17-11441-2017>, 2017.

707 Zhang, X., Trzepla, K., White, W., Raffuse, S., and Hyslop, N. P.: Intercomparison of thermal–optical carbon measurements by Sunset and Desert Research
708 Institute (DRI) analyzers using the IMPROVE_A protocol, *Atmos. Meas. Tech.*, 14, 3217-3231, <https://doi.org/10.5194/amt-14-3217-2021>, 2021.

709 Zhu, J., Crozier, P. A., and Anderson, J. R.: Characterization of light-absorbing carbon particles at three altitudes in East Asian outflow by transmission electron
710 microscopy, *Atmos. Chem. Phys.*, 13, 6359-6371, <https://doi.org/10.5194/acp-13-6359-2013>, 2013.

711 Zotter, P., Herich, H., Gysel, M., El-Haddad, I., Zhang, Y., Močnik, G., Hüglin, C., Baltensperger, U., Szidat, S., and Prévôt, A. S. H.: Evaluation of the
712 absorption Ångström exponents for traffic and wood burning in the Aethalometer-based source apportionment using radiocarbon measurements of ambient
713 aerosol, *Atmos. Chem. Phys.*, 17, 4229-4249, <https://doi.org/10.5194/acp-17-4229-2017>, 2017.

714

715

716 **Table 1.** Classification of the campaign period during May 05–June 09, 2021.

Name	Date	Cruise route	Monsoon	Wind direction
BMP-1	May 05–09	AB	before	0–90°, northeast
BMP-2	May 10–22	B→C→D	before	90–180°, southeast
BMP-3	May 23–26	D→E	before	around 180°, southeast
TMP	May 27–Jun 01	EB	transition	around 180°, south
AMP	June 02–09	B→D→A	after	180–270°, southwest
SPP*	Screened	Screened	N/A	Screened

717 * Ship pollution period is screened based on BC concentration and relative wind direction as mentioned in the method section.

718

719 **Table 2.** Source apportionment of BC based on the two-component AAE model.

Period	a.BC(FF)* ($\mu\text{g m}^{-3}$)	a.BC(BB)* ($\mu\text{g m}^{-3}$)	r.BC(BB)* ($\mu\text{g m}^{-3}$)	r.BC(FF)* ($\mu\text{g m}^{-3}$)	f.BC(FF)* (%)	f.BC(BB)* (%)
BMP	0.2 ± 0.1	0.08 ± 0.06	0–0.9	0–0.3	77.9 ± 5.8	22.1 ± 5.8
TMP	0.2 ± 0.3	0.06 ± 0.1	0.02–1.8	0–1.1	82.2 ± 6.2	17.8 ± 6.2
AMP	0.2 ± 0.1	0.05 ± 0.05	0.01–0.9	0–0.3	80.8 ± 4.0	19.2 ± 4.0
SPP	4.4 ± 5.7	0.7 ± 0.9	0.2–32.8	0.04–10.3	83.0 ± 6.7	17.0 ± 6.7
Bio. **	0.8 ± 0.3	0.8 ± 0.4	0.05–1.2	0–1.5	58.1 ± 16.7	41.9 ± 16.7

720 * a represents average, r for range, f for fraction;

721 ** Bio. stands for the two biomass burning events as noted in the main text.

722

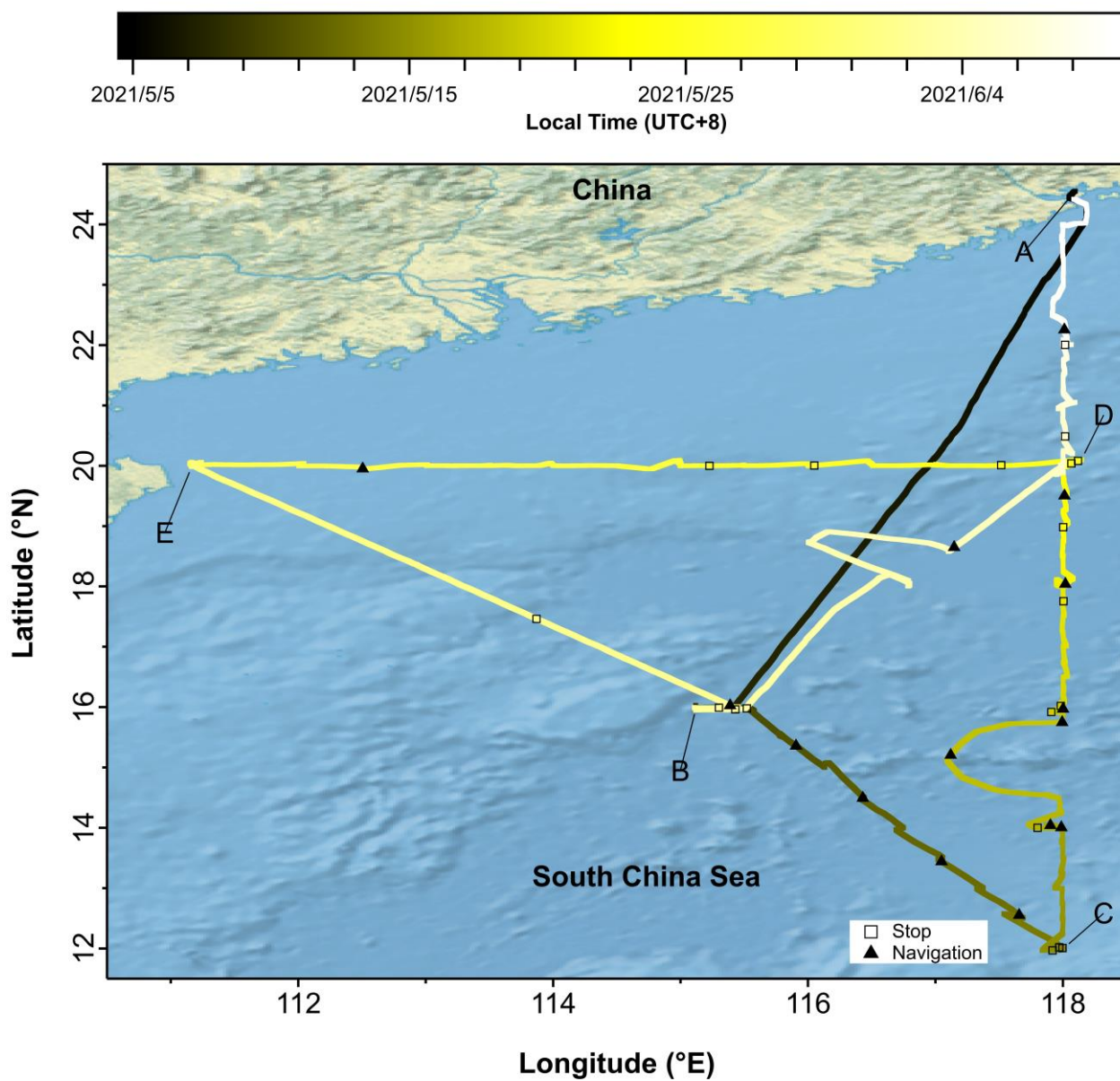
723 **Table 3.** Summary of AAE values, mass concentrations, and the relevant fractions for the BC particles in PM_{2.5} from coast site and cruise measurements using
 724 the AE series aethalometer.

Region	Time	AAE values (at wavelengths, nm)	BC avg. conc. ($\mu\text{g m}^{-3}$)	Fraction (%)	Reference
East China Sea ^c	May, 2017	0.9–1.3 (370–950)	0.8–3.6	2.5–11 or 45–60 for BrC	(Yu et al., 2018)
Central Adriatic ^c	Feb.–Jul., 2019	1.25–1.49 (470/950)	0.57 ± 0.64	79 for BC(FF) 21 for BC(BB)	(Milinković et al., 2021)
Bay of Bengal ^{c, n}	Dec., 2008–Jan., 2009	1.81–1.98 (370–950)	5.1 ± 3.0 ^c ; 2.5 ± 1.4 ⁿ	<10 for BC(FF) >85 for BC(BB)	(Kedia et al., 2012)
South China Sea ⁿ	Sep.–Oct. 2019	-	1.9 ± 0.4	-	(Wang et al., 2022)
South China Sea ^c	Dec. 2017	1.2–1.5 (375/880)	6.6–4.9	-	(Sun et al., 2020c)
South China Sea ⁿ	May–Jun. 2021	1.02–1.14 or 1.93 (370–950)	0.33 ± 0.38	78–82 for BC(FF) 18–22 for BC(BB) BB events: 58 for BC(FF) 42 for BC(BB)	This study

725 ^c coastal site measurement;

726 ⁿ cruise (remote) measurement.

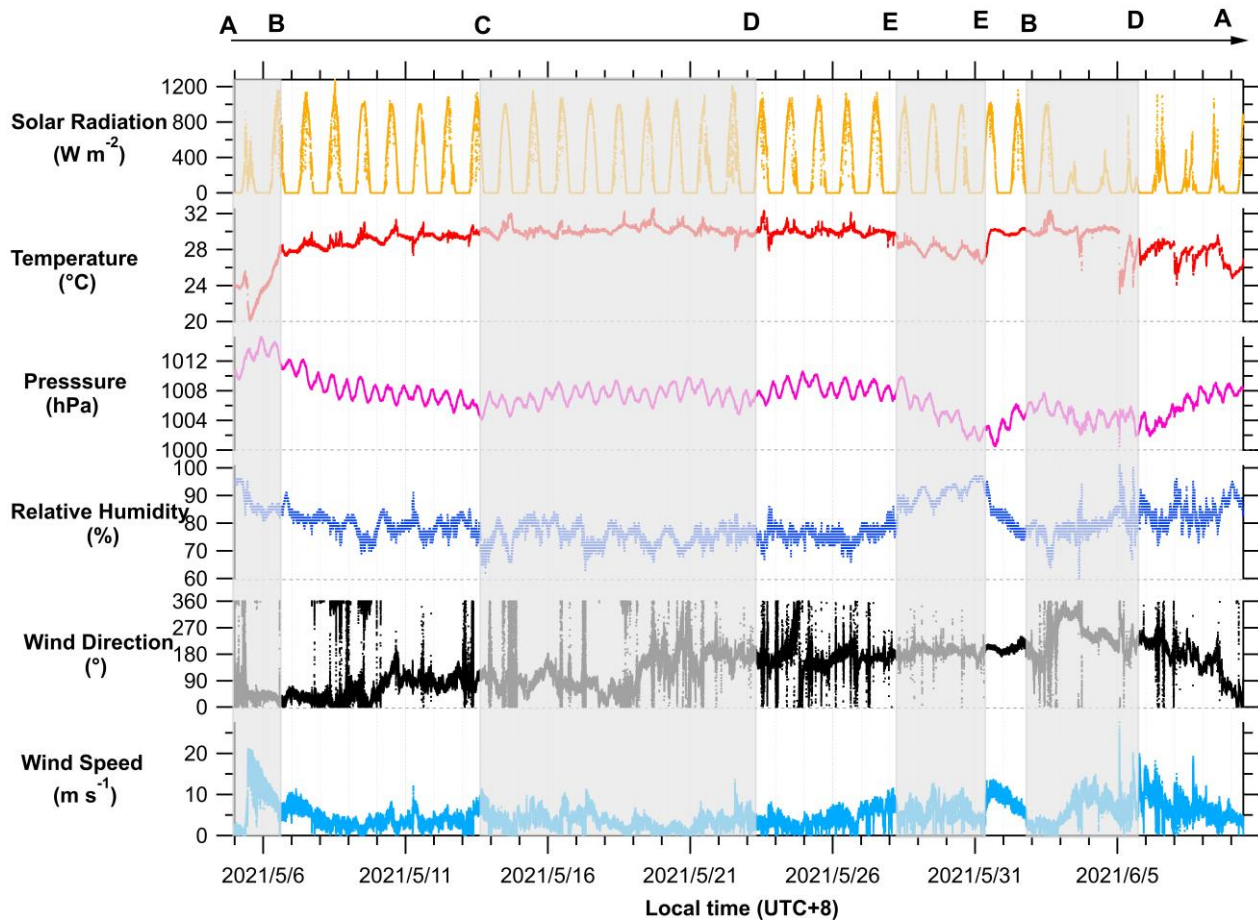
727



728

729 Figure 1. Map of the cruise route for the campaign in the South China Sea during May 05–Jun 9, 2021. The ship route is dated by the intensity bar at the top. The open

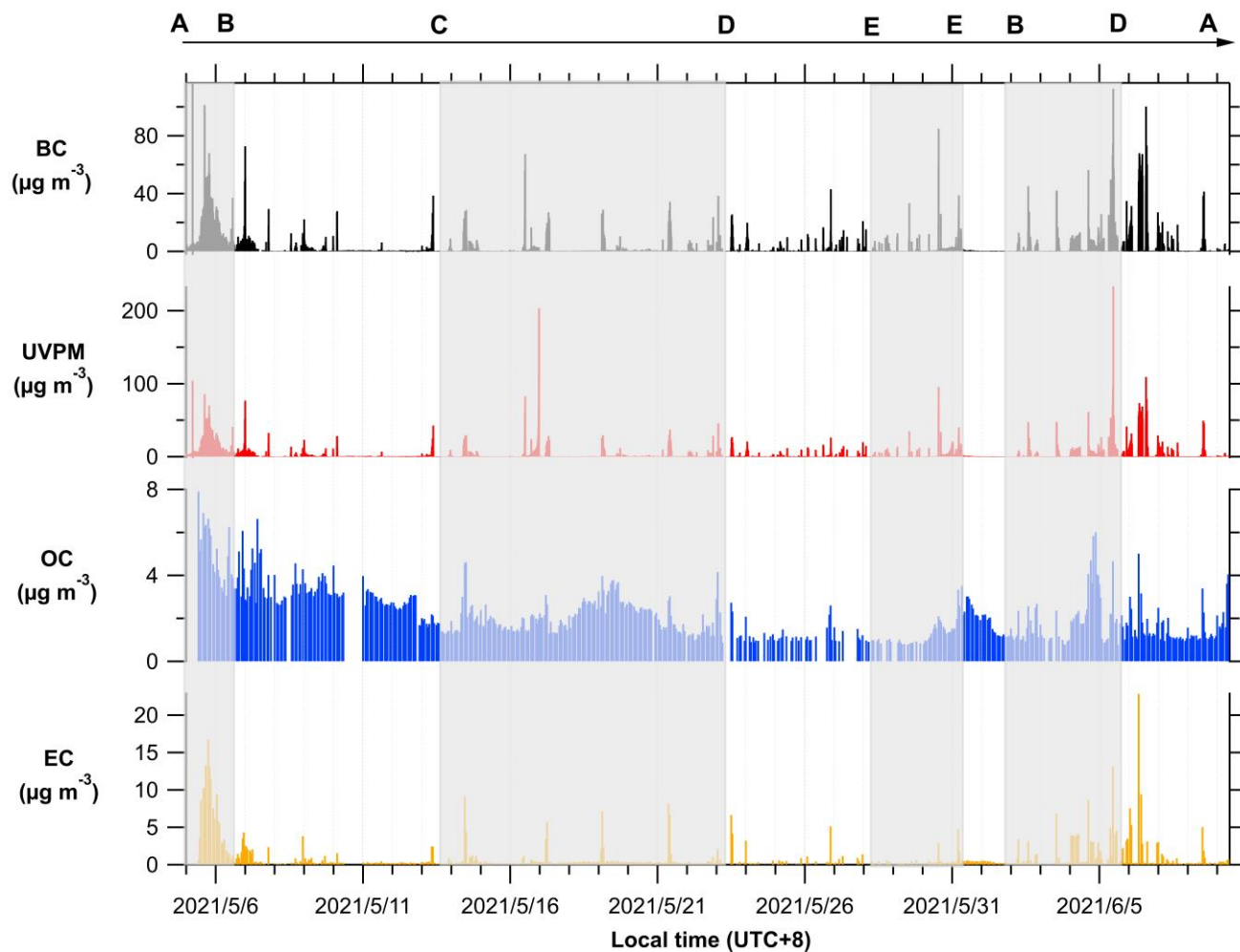
730 squares and solid triangles indicate the single particle sampling location, collected during stop and navigation, respectively.



731

732 **Figure 2.** Time series of meteorological variables of solar radiation (SR), temperature, pressure, relative humidity (RH), wind direction (WD), and wind speed (WS)
 733 during the campaign. The time resolution is 1 min for all the data except for WS and WD (3 sec). All data points are shown in dots style. The shaded and unshaded areas
 734 sequentially indicate the cruise routes from AB, B to C, C to D, D to E, E to E (ship stop), E to B, B to D, and D to A, as marked in the Figure 1.

735

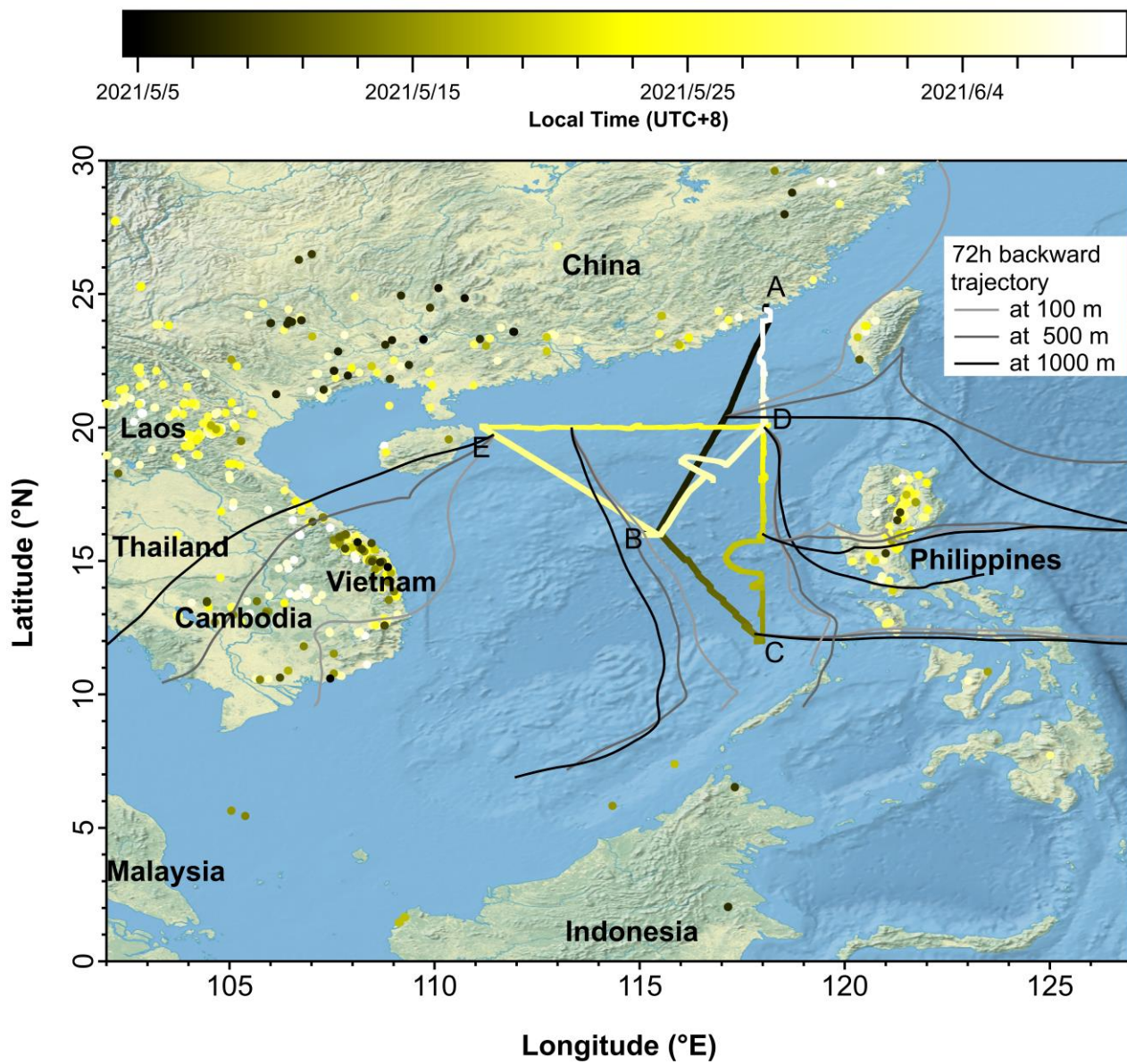


736

737 **Figure 3.** Time series of the mass concentration of black carbon (BC), ultraviolet particle matter (UVPM), organic carbon (OC) and elemental carbon (EC) in $PM_{2.5}$

738 during the campaign. The time resolution is 1 min for all the data except for OC and EC (1 h). All data points are shown in stick-to-zero style. The shaded and unshaded

739 areas sequentially indicate the cruise routes from AB, B to C, C to D, D to E, E to E (ship stop), E to B, B to D, and D to A, as marked in the Figure 1.



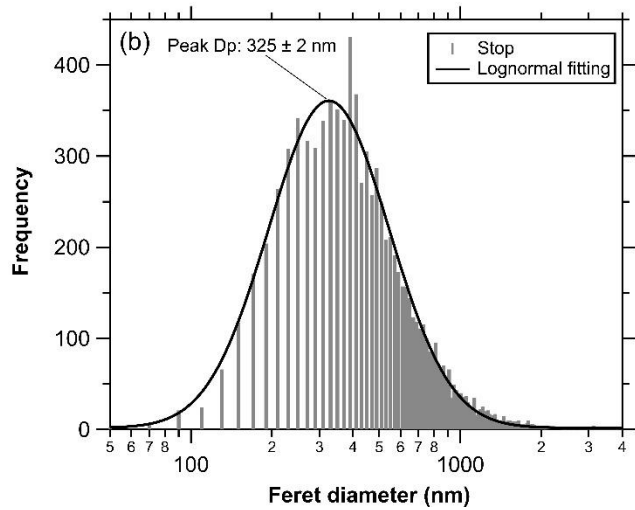
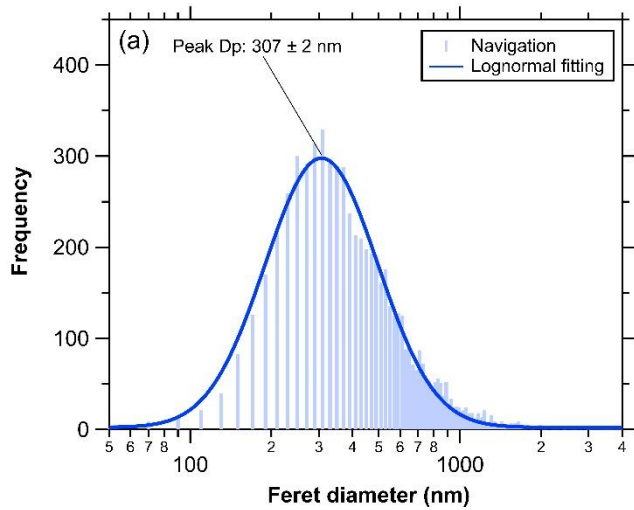
740

741 Figure 4. The time series of fire spots distribution and the 72-h backward trajectories over the South China Sea (SCS) during the campaign. The solid circles were dated

742 by the intensity bar at the top, representing the detected fire spots using MODIS satellite with a confidence threshold of >80%. The light grey, grey and black 72-h

743 backward trajectories were obtained at AGL heights of 100, 500 and 1000 m using the HYSPLIT model.

744



745

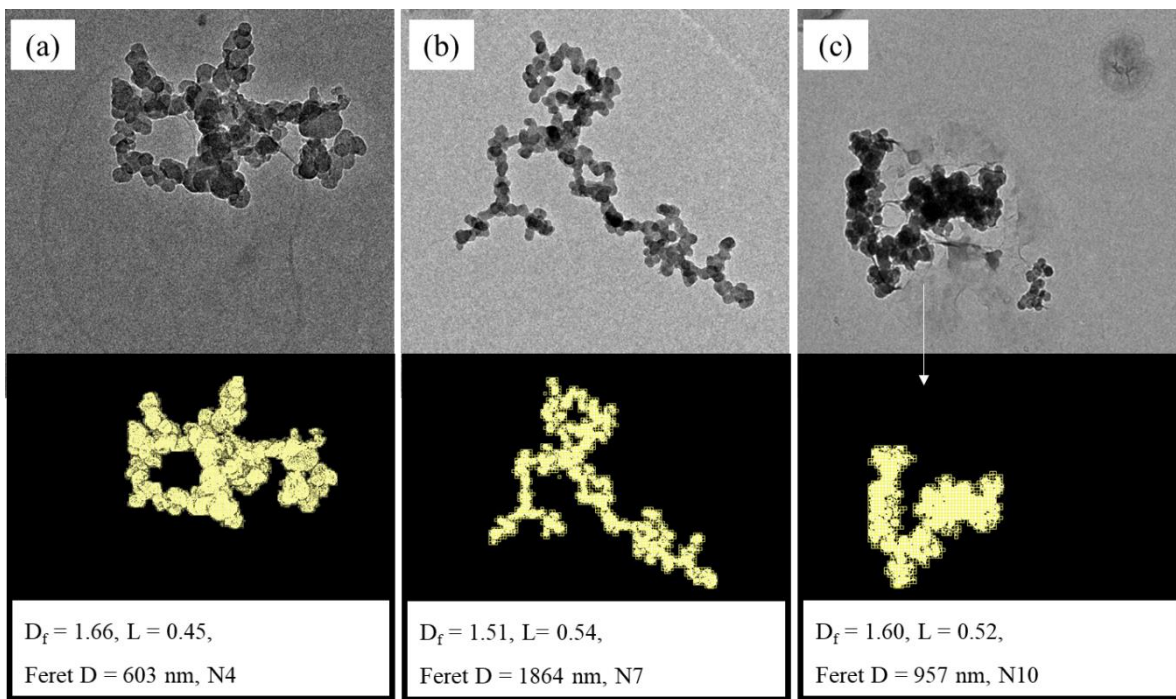
746 **Figure 5. Lognormal fitting of particle size distribution using Feret diameter determined from the TEM images with the ImageJ analysis during navigation (a) and stop**

747 (b). The histograms are set with a bin starting at 50 nm, a bin width of 20 nm, and a total bin number of 200.

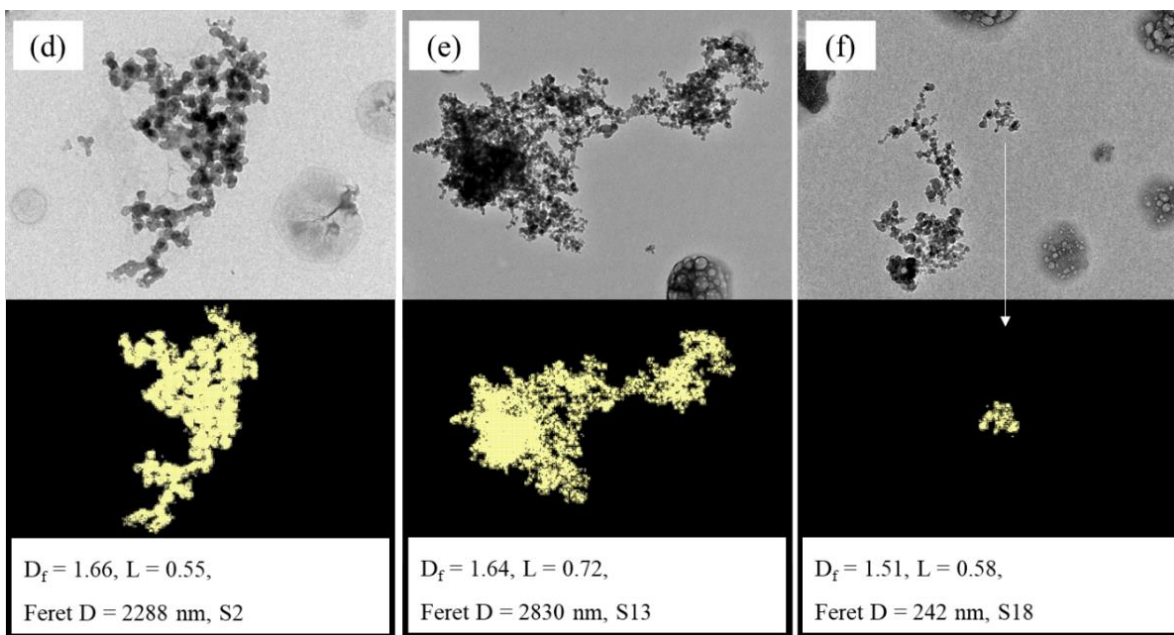
748

749

750



751

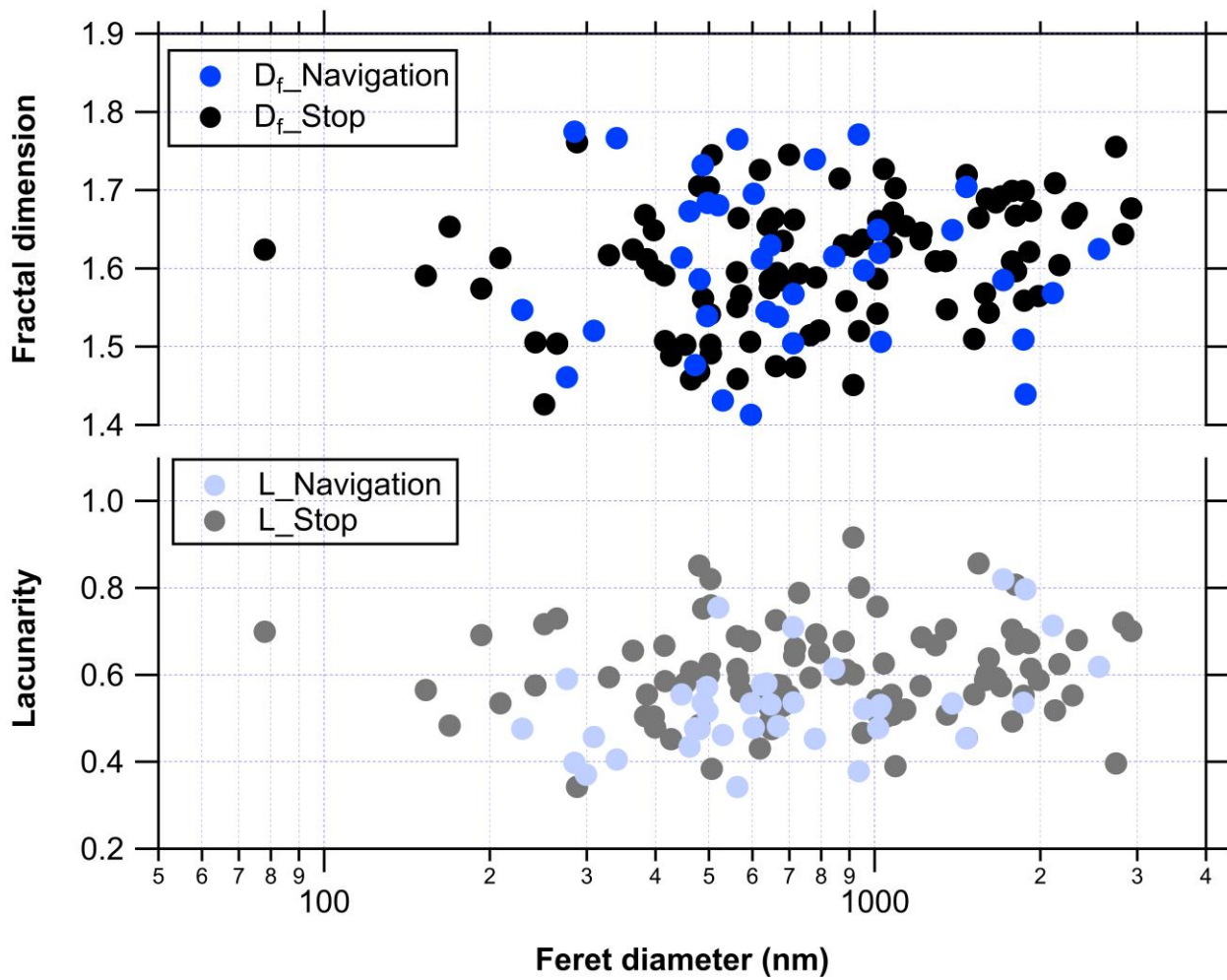


752

753 **Figure 6.** Examples of the BC TEM images and their corresponding Feret diameter (D), fractal dimension (D_f) and Lacunarity (L) based on the boxing counting

754 method from the fractal analysis: (a-c) BC particles collected during navigation and (d-f) during stop. More sampling information can be found in Table S1 of SI (serial

755 numbers N4, N7, N10, S2, S13, S18, etc.).

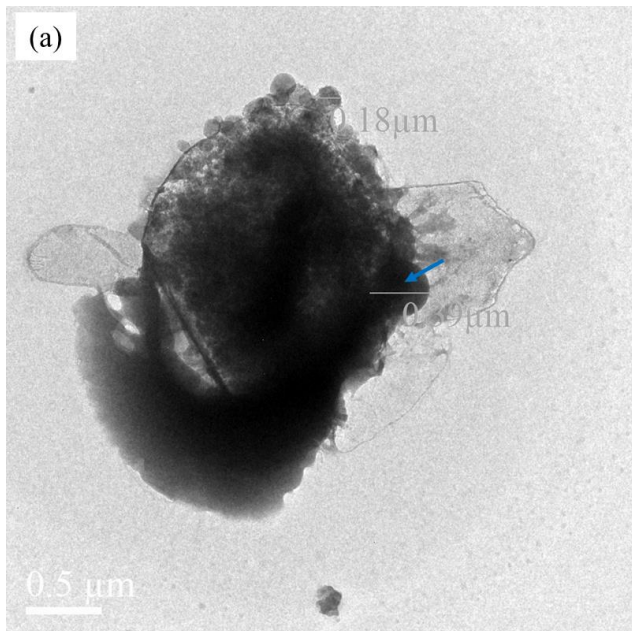


756

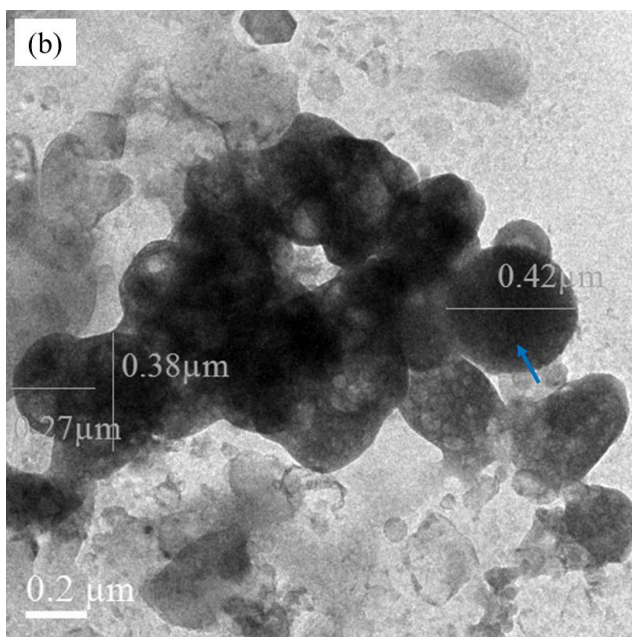
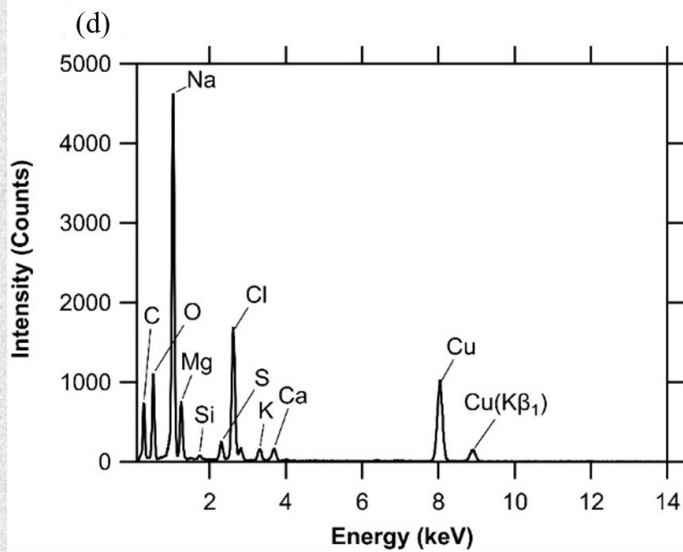
757 **Figure 7.** The size-dependent fractal dimension (D_f) and lacunarity (L) for each BC particle during navigation and stop. A total number of 134 data points are shown in

758 **Figure 6.**

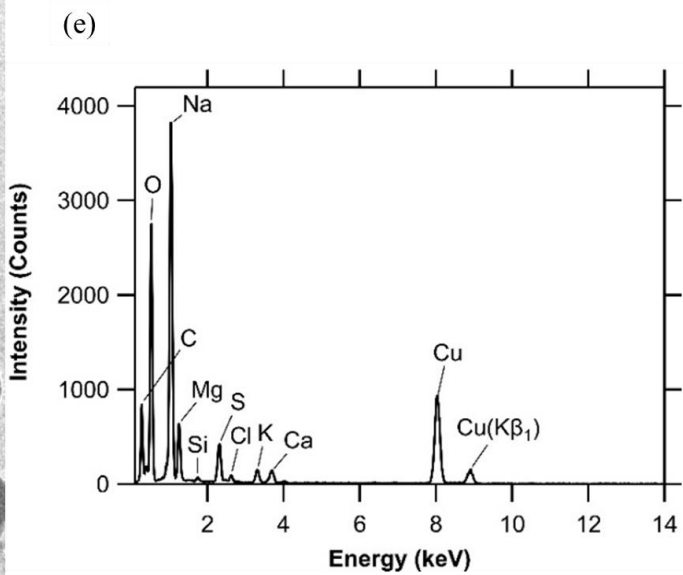
759

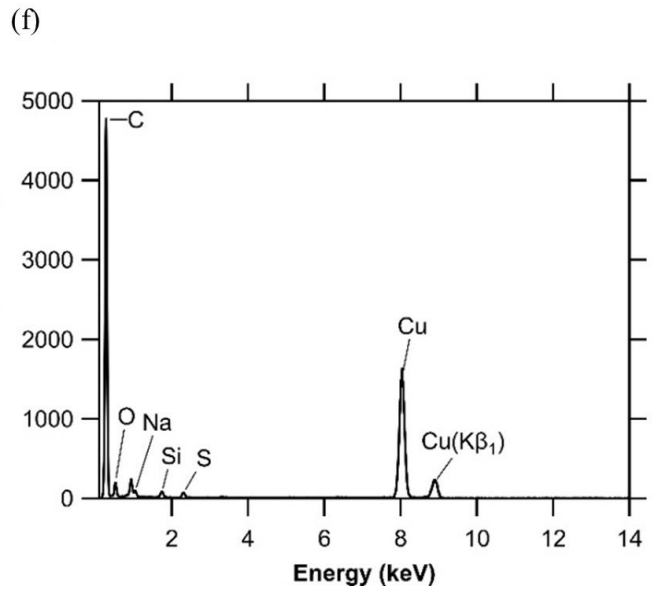
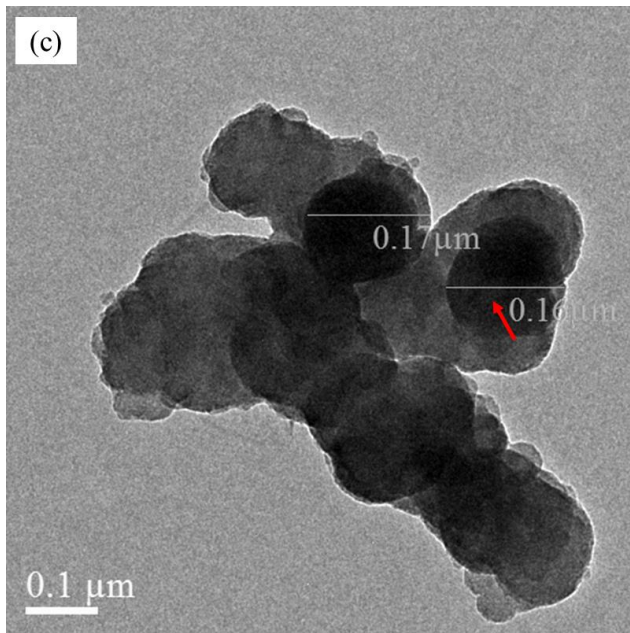


760



761





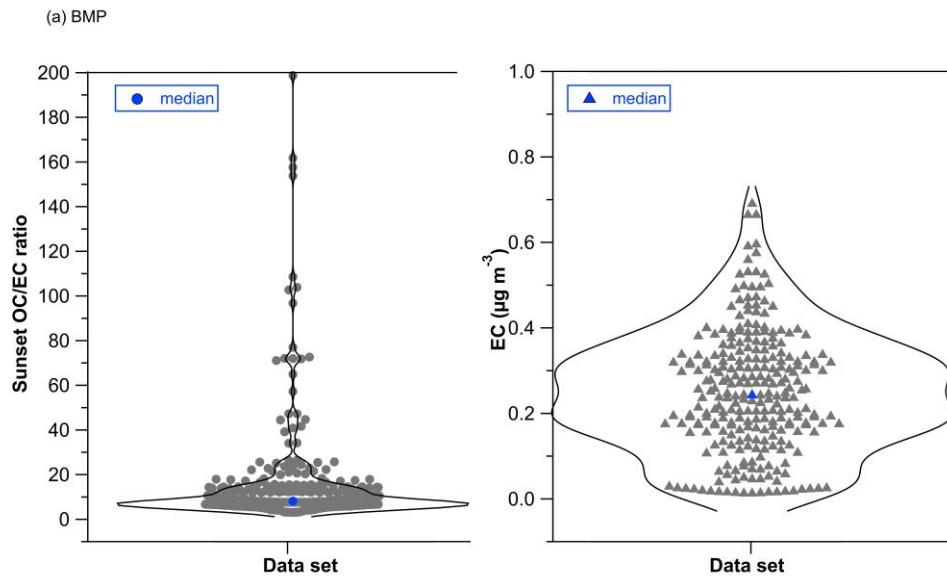
762

763 **Figure 8.** The example TEM images and their corresponding EDS spectra of particles collected during navigation: tar balls mixed with sea salt (a, d) at 8:55 on May 27,

764 tar balls mixed with OC, sulfate (b, e), and amorphous carbon agglomerates mixed with sulfate (c, f) at 18:07 on Jun 01. The EDS spectra were collected by focusing the

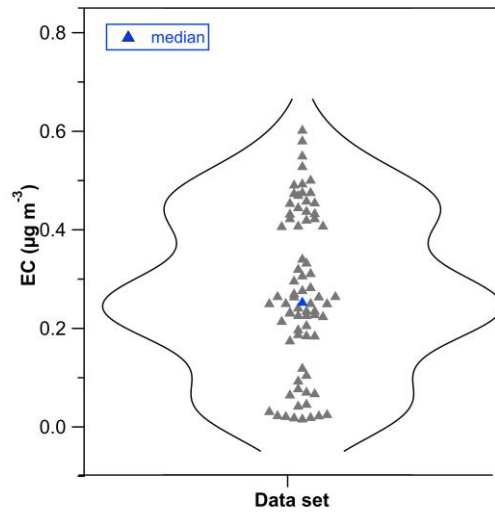
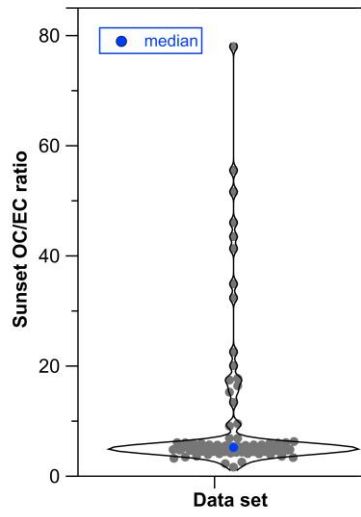
765 electron beam in the TEM and the illuminated area covers the center of the particle for elemental analysis. The blue arrows indicate tar balls and the red arrow indicates

766 amorphous carbon. The EDS is obtained from beam focus on the center of the particle.



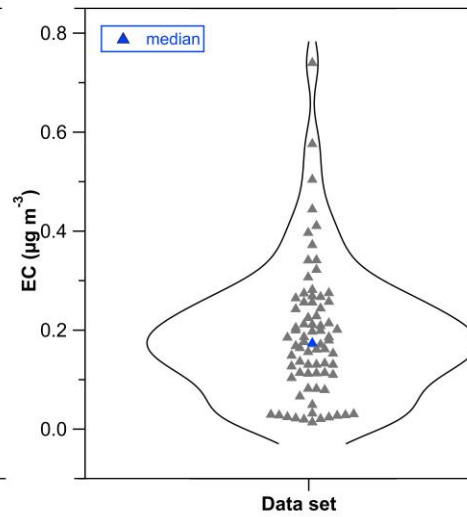
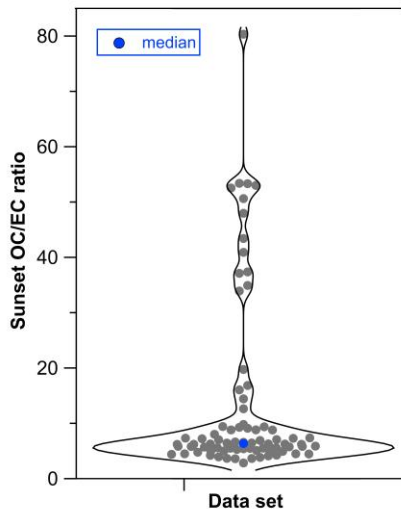
767

(b) TMP



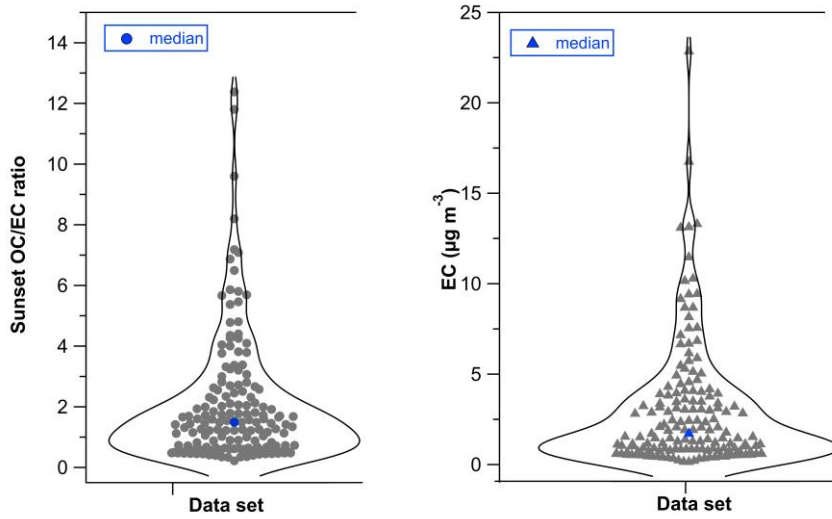
768

(c) AMP



769

(d) SPP



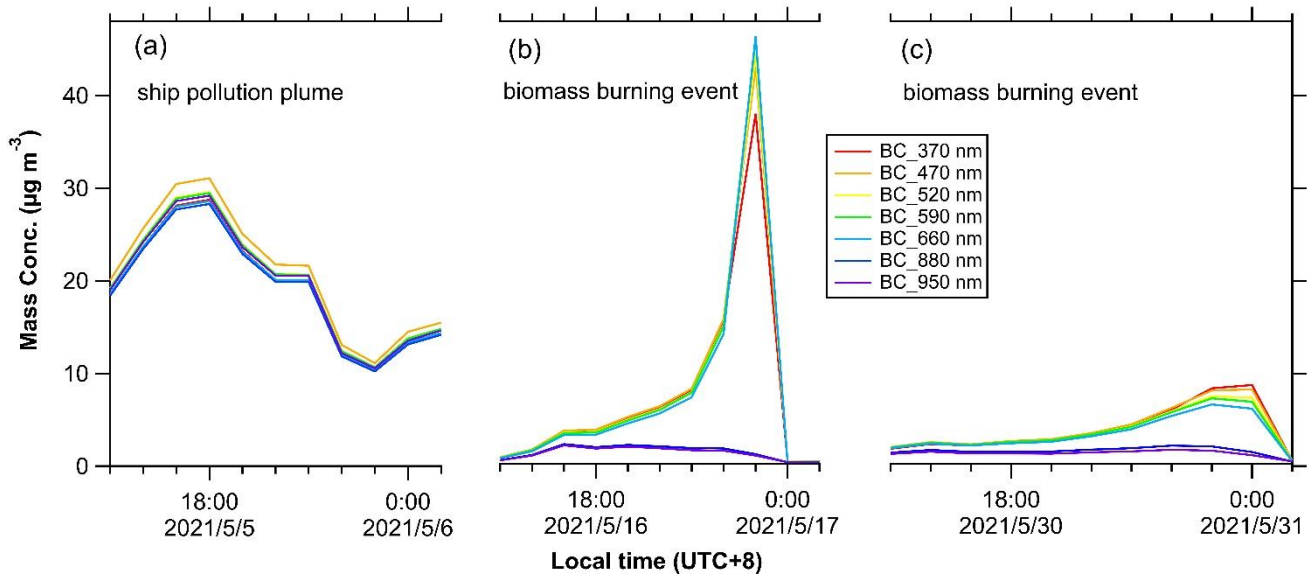
770

771 **Figure 9.** Violin plots of the OC/EC ratios and EC concentrations for (a) before the monsoon period (BMP), (b) transition monsoon period (TMP), (c) after the monsoon

772 period (AMP), and (d) ship pollution period (SPP) based on the data from the Sunset OC/EC analyzer. The blue solid circles and triangles indicate median values of

773 Sunset OC/EC ratios and EC mass concentrations, respectively. The total data points are 551 in the data set, with a concentration range of 0.76-7.90 $\mu\text{g m}^{-3}$ for OC and

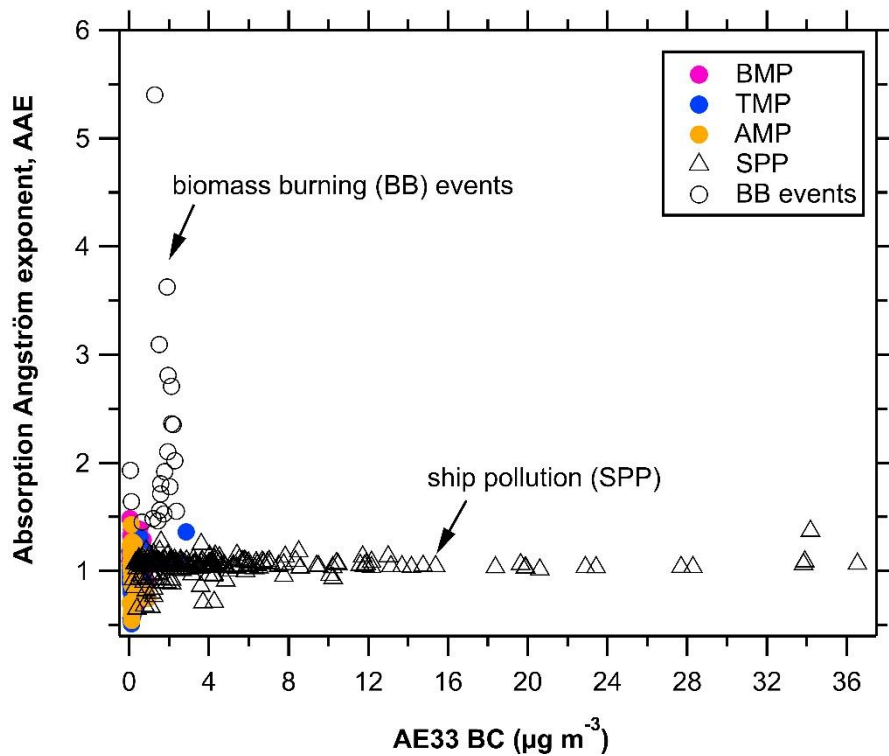
774 0.013-22.84 for EC $\mu\text{g m}^{-3}$. Particularly, all OC data is above LOD of 0.18 $\mu\text{g m}^{-3}$ while 29% of EC data is below LOD of 0.19 $\mu\text{g m}^{-3}$.



775

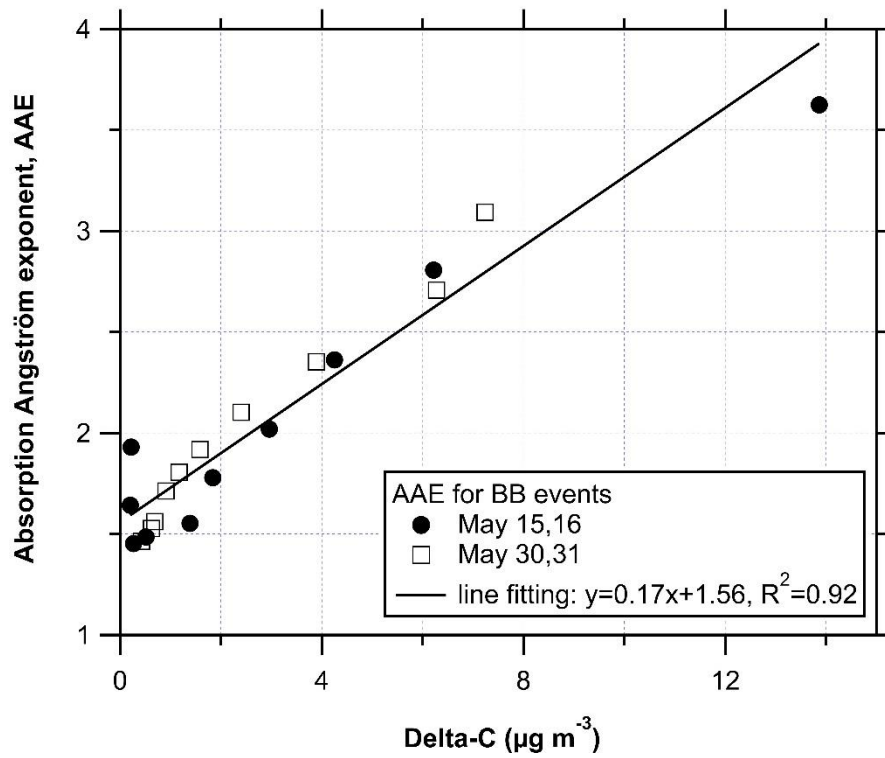
776 Figure 10. The wavelength-dependent mass concentration from AE33 aethalometer for example spectra for (a) example of a ship pollution plume, and (b, c) two
777 significant biomass burning events during this campaign.

778



779

780 Figure 11. The absorption Angström exponent (AAE, all wavelengths) vs AE33 BC concentration for before monsoon period (BMP), transition monsoon period (TMP),
781 after monsoon period (AMP), and ship pollution period (SPP).

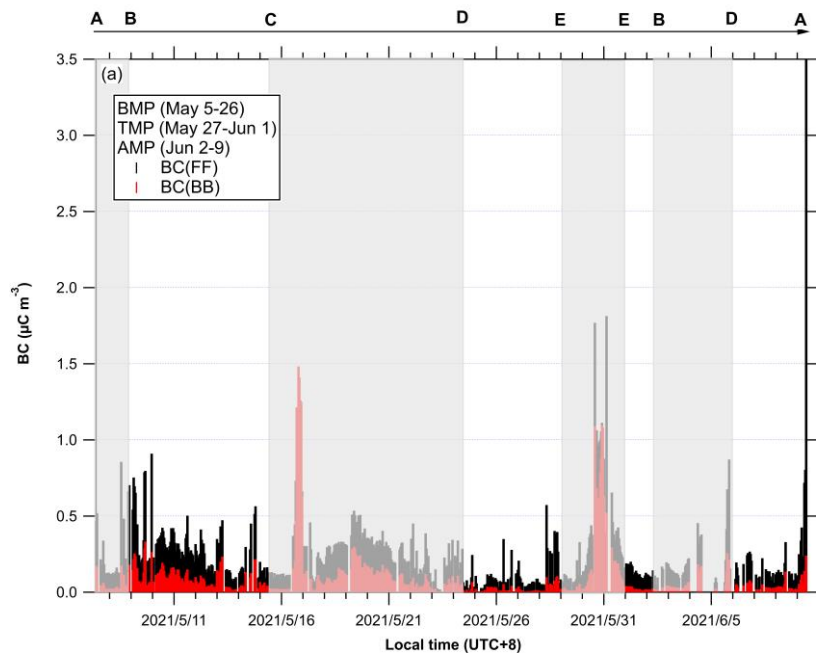
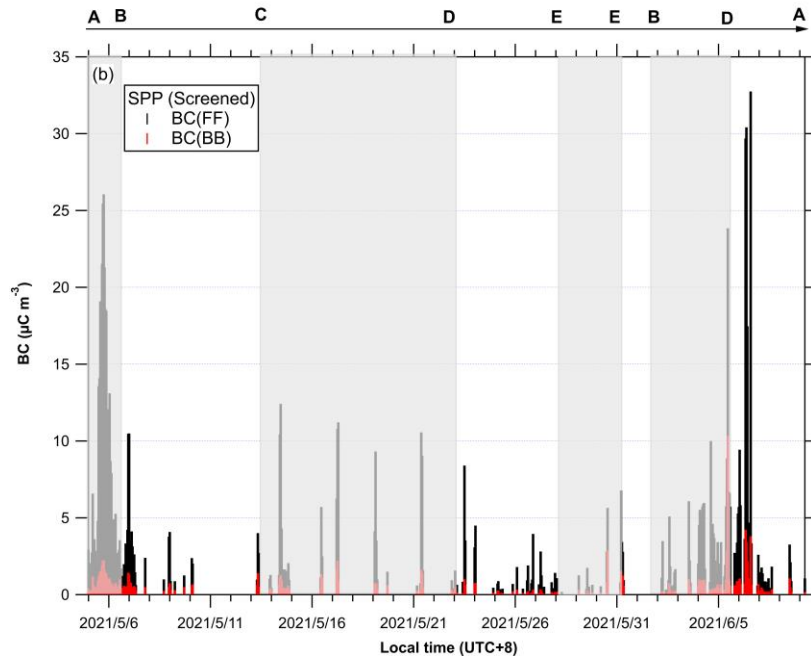


782

783 **Figure 12.** The absorption Angström exponent (AAE) vs the Delta-C concentration for the two biomass burning events: BB-1 at 6:00–7:00 on May 15 and 15:00–22:00

784 on May 16 during BMP, and BB-2 at 15:00–23:00 on May 30 and 00:00 on May 31 during TMP. The BB-1 and BB-2 data points are marked in solid circles and open

785 squares, respectively.



786

787

788 **Figure 13.** Source apportionment of the BC particles using the two-component AAE model (AAE=1 for foil fuel (FF) and AAE=2 for biomass burning (BB)): (a) before
 789 monsoon period (BMP), transition monsoon period (TMP), after monsoon period (AMP), and (b) ship pollution period (SPP). The shaded and unshaded areas
 790 sequentially indicate the cruise routes from AB, B to C, C to D, D to E, E to E (ship stop), E to B, B to D, and D to A, as marked in Figure 1.